Tectonics

RESEARCH ARTICLE
10.1029/2019TC005933

Key Points:
- We use satellite topography and a numerical model to analyze normal fault scarps and knickpoints potentially reflecting multiple earthquakes
- The Bilila-Mtakataka fault, Malawi, shows evidence for two previous ruptures with 10–12 m of vertical offset each
- The degradation of the scarps suggests a diffusion age of 48 ± 25 m^2 corresponding to 6.4 ± 4.0 Kyr since formation

Supporting Information:
- Figure S1

Correspondence to:
J. Biggs,
juliet.biggs@bristol.ac.uk

Citation:
Hodge, M., Biggs, J., Fagereng, Å., Mdala, H., Wedmore, L. N. J., & Williams, J. N. (2020). Evidence from high-resolution topography for multiple earthquakes on high slip-to-length fault scarps: The Bilila-Mtakataka fault, Malawi. *Tectonics*, *39*, e2019TC005933. https://doi.org/10.1029/2019TC005933

Received 19 NOV 2019
Accepted 17 DEC 2019
Accepted article online 18 DEC 2019

Evidence From High-Resolution Topography for Multiple Earthquakes on High Slip-to-Length Fault Scarps: The Bilila-Mtakataka Fault, Malawi

M. Hodge[1], J. Biggs[2], Å. Fagereng[1], H. Mdala[3], L. N. J. Wedmore[2], and J. N. Williams[1]

[1]School of Earth and Ocean, Cardiff University, Cardiff, UK, [2]School of Earth Sciences, University of Bristol, Bristol, UK, [3]Geological Survey Department, Zomba, Malawi

Abstract Geomorphological features such as fault scarps and stream knickpoints are indicators of recent fault activity. Determining whether these features formed during a single earthquake or over multiple earthquakes cycles has important implications for the interpretation of the size and frequency of past events. Here, we focus on the Bilila-Mtakataka fault, Malawi, where the 20 m high fault scarps exceed the height expected from a single earthquake rupture. We use a high-resolution digital elevation model (<1 m) to identify complexity in the fault scarp and knickpoints in river profiles. Of 39 selected scarp profiles, 20 showed evidence of either multiscarps or composite scarps, and of the seven selected river and stream profiles, five showed evidence for multiple knickpoints. A near-uniform distribution of vertical offsets on the subscarps suggests they were formed by separate earthquakes. These independent methods agree that at least two earthquakes have occurred with an average vertical offset per event of 10 and 12 m. This contrasts earlier studies which proposed that this scarp formed during a single event and demonstrates the importance of high-resolution topographic data for understanding tectonic geomorphology. We use a one-dimensional diffusion model of scarp degradation to demonstrate how fault splays form multiscarps and estimate the diffusion age κt of the Bilila-Mtakataka fault scarp to be 48 ± 25 m^2, corresponding to $6,400 \pm 4,000$ years since formation. We calculate that a continuous rupture would equate to a M_W 7.8 ± 0.3 earthquake, greater than the largest seismic event previously recorded in East Africa.

1. Introduction

Historical and instrumental catalogs alone provide a short and incomplete record of past earthquakes (e.g., Hodge et al., 2015; McCalpin, 2009), and devastating earthquakes may occur on faults that have no historical earthquake activity (e.g., 2003 M_W6.6 Bam earthquake in Iran; Fu et al., 2004). By investigating fault-generated landforms such as fault scarps, an assessment of the earthquake and rupture history along a fault, and the probability and hazard of future earthquakes, can be made (e.g., Andrews & Hanks, 1985; Bucknam & Anderson, 1979; Duffy et al., 2014; Hanks et al., 1984; Nash, 1980; Wallace, 1977; Zhang et al., 1991; Zielke et al., 2015). Paleoseismological trenching can provide information about timing and magnitude of prehistoric earthquakes (e.g., Michetti & Brunamonte, 1996; Palyvos et al., 2005; Schwartz & Coppersmith, 1984), but trenching requires particular geomorphic conditions and is limited by site accessibility.

Estimates of the displacement and age of earthquake ruptures can be made from geomorphical analyses of fault scarps and river channels (e.g., Avouac, 1993; Bucknam & Anderson, 1979). The latest generation of satellite-derived digital elevation models (DEMs) have sufficient resolution for these estimates to be made remotely (Figure 1). In cases where there are subtle changes in morphology, such as slope breaks within the fault scarp, the existence of multiple ruptures can be analyzed (Wallace, 1980, 1984) for comparison with other paleoseismological records (Ewiak et al., 2015). Furthermore, along-strike comparisons, which are not possible with point sampling methods such as trenching, can be used to analyze the structural evolution of the fault (e.g., Crone & Haller, 1991; Hodge et al., 2018b, 2019; Manighetti et al., 2005; Perrin et al., 2016a). Rivers and streams crossing fault scarps may also preserve indicators of past earthquakes in the form of vertical steps—called knickpoints—in an otherwise convex and smooth longitudinal profile (e.g., Burbank & Anderson, 2011; Holbrook & Schumm, 1999; Ouchi, 1985; Wei et al., 2015). These can be used to identify

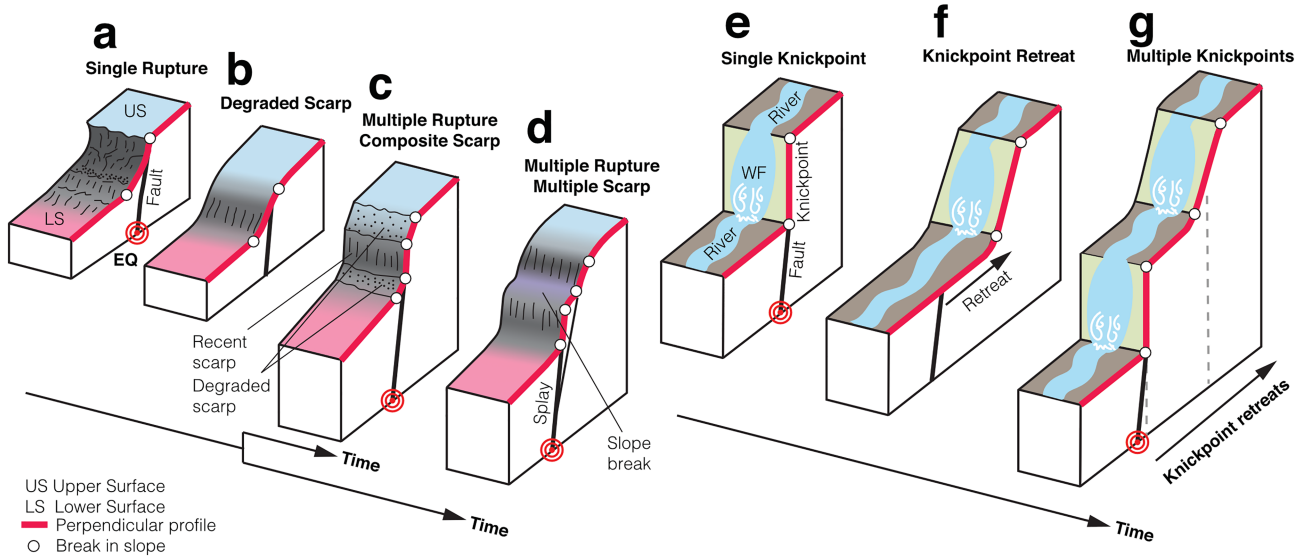

Figure 1. Various geomorphic indicators of multiple ruptures in an idealized system assuming no lithological contrasts or bedrock fabric. (a) A single rupture scarp, where the upper original surface (US) and lower original surface (LS) are separated by a scarp formed of a steep free face, and wash and debris faces. The elevation profile (red line) shows two prominent changes in slope marked by breaks in slope (white circles). (b) A degraded scarp. Erosion and deposition of material smooths the scarp surface. Following another surface rupture, either (c) a composite scarp forms, where the most recent rupture is indicated by a steeper slope on the scarp surface; or (d) a multiscarp forms where individual scarps are separated by a break in slope. These may form in either single or multiple earthquakes. (e) A knickpoint forms during a rupture. (f) Between rupture events the knickpoint retreats upstream. (g) Another knickpoint forms following a subsequent rupture. The knickpoints are separated by reaches of the river which are at their equilibrium gradient.

active fault traces in regions with complex topography (Litchfield et al., 2003) and for paleoseismological analysis (Ewiak et al., 2015; Wei et al., 2015).

In this study, we investigate whether indicators of multiple ruptures exist along two major structural segments of the Malawi Rift's Bilila-Mtakataka fault (BMF). Earlier studies suggested that the scarp may reflect a single earthquake that ruptured the whole along-strike extent of the fault (Jackson & Blenkinsop, 1997). However, more recent studies indicate that the fault scarp has a higher degree of along-strike structural complexity and actually consists of at least six geometrically distinct segments (Goda et al., 2018; Hodge et al., 2018b). UAV data collected on recent field visits also show that the scarp is more complex than previously described, at least in the few accessible localities.

Here we use a very high-resolution (<1 m) point cloud and DEM to detect changes or breaks in slope on individual scarp profiles and use knickpoint analysis to estimate the number of ruptures that may have occurred on each segment. In addition, we use the fault scarp morphology and knickpoint height to estimate the surface offset associated with each event. We then apply a model of scarp degradation to estimate the diffusion age κt of the scarp profiles, that is, the amount of erosion that has occurred at the scarp's crest since the scarp's formation. Diffusion age κt, having dimension [length]^2, is the product of diffusivity and chronological age (Andrews & Hanks, 1985). If we assume the diffusivity is constant, this allows us to infer the relative timing of each rupture, and by selecting a typical diffusion constant κ of the region, we can convert diffusion age to chronological age t. Finally, we discuss the processes that formed the current BMF scarp and consider future rupture scenarios.

2. Geomorphic Indicators of Multiple Ruptures

2.1. Complex Fault Scarps

The morphology of a fault scarp is dependent on many factors, including the type of earthquake, amount of slip, and the material properties of the surface it displaces. Typically, a single rupture fault scarp will comprise a free face whose gradient is greater than the angle of repose of the hillslope sediments (Lin et al., 2017; Nash, 1984; Wallace, 1977; e.g., Figure 1a). These distinctive free faces, however, erode away within a few hundred years (e.g., Bucknam & Anderson, 1979; Nash, 1984; Wallace, 1980), forming smoother, degraded scarp profiles (Figure 1b). When more than a single surface rupture has occurred along a fault, the scarps may comprise either a single scarp face with differing slopes within it or an array/stack of multiple discrete

scarps set back from one another (Crone & Haller, 1991; Ganas et al., 2005; Nash, 1984; Wallace, 1977; Zhang et al., 1991). Composite scarps comprise a single band of oversteepened terrain where vertical offsets have accumulated onto the same slope over multiple earthquake cycles (Ganas et al., 2005; Zhang et al., 1991; e.g., Figure 1c), whereas the vertical offsets of multiscarps are horizontally offset by terraces (e.g., Crone & Haller, 1991; Nash, 1984). Composite fault scarps develop when near-surface slip is confined to the same fault plane, but multiscarps form when slip is confined to a different near-surface fault splay during each earthquake event (e.g., Anders & Schlische, 1994; Kristensen et al., 2008; Nash, 1984; Slemmons, 1957). Both multiscarps and composite scarps can exist along the same fault if a splay is reactivated as shown in the Serghaya Fault Zone, Syria (Gomberg et al., 2001), the northern Upper Rhine Graben, Germany (Peters & van Balen, 2007), and northern Baja California, Mexico (e.g., Mueller & Rockwell, 1995).

Multiple surface ruptures on composite scarps may be identified by changes in scarp slope, marked by slope breaks on the scarp's elevation profile (Figure 1c; e.g., Lin et al., 2017; Nash, 1984); however, as the scarp degrades, these multiple rupture markers will disappear over time (e.g., Bucknam & Anderson, 1979; Nash, 1984; Wallace, 1980). The terraces between individual scarps on a multiscarp (Mayer, 1982; e.g., Figure 1d) provide a more lasting record of earthquake activity, but multiscarps too are considered to degrade to a morphology similar to a degraded single rupture fault scarp over sufficient timescales (e.g., Andrews & Hanks, 1985; Nash, 1984). Understanding whether multiple earthquake ruptures have occurred on a fault scarp is important as surface displacements may be used in quantifying paleomagnitude estimates for faults (e.g., Swan et al., 1980; Walker et al., 2015; Wei et al., 2015), and overestimating slip per earthquake will influence recurrence interval calculations and thus the inferred seismic hazard (e.g., Middleton et al., 2016).

2.2. Knickpoints

The offset produced by surface ruptures also generates a change in fluvial systems. Studying the topographical variations within bedrock rivers has been an effective tool in understanding the evolution of tectonically active landscapes (e.g., Finlayson et al., 2002; Montgomery & Brandon, 2002). In fluvial geomorphology, the change in the appearance of a river's longitudinal profile can be a response to tectonic activity (e.g., Burbank & Anderson, 2011; Holbrook & Schumm, 1999; Litchfield et al., 2003; Ouchi, 1985; Wei et al., 2015). Typically, the longitudinal profile is smooth and concave in appearance; however, in bedrock channels, surface ruptures can produce knickpoints (Figure 1e; e.g., Commins et al., 2005; He & Ma, 2015; Sun et al., 2016; Wallace, 1977; Yang et al., 1985). Over time, knickpoints retreat upstream from their original position during the process of channel regrading (Figure 1f). As knickpoints migrate upstream, they reduce in height and may eventually disappear (Holland & Pickup, 1976). Subsequent surface ruptures can cause additional knickpoints to develop, separated by reaches of the river which are at their equilibrium gradient (Figure 1g).

If the retreat rate is known, the age of formation can be calculated by measuring the retreat distance, and the knickpoint height may be used (assuming rupture area is known) to estimate the magnitude of each earthquake event (e.g., Castillo, 2017; He & Ma, 2015; Rosenbloom & Anderson, 1994; Sun et al., 2016; Wei et al., 2015). However, numerical models and field observations have shown that many complex processes including sediment flux, channel morphology, channel slope, and drainage area contribute to the rate of knickpoint retreat (Attal et al., 2008, 2011; Cowie et al., 2006; Gasparini et al., 2006; Whittaker et al., 2007a, 2007b). In the past, analysis of knickpoints was a field-based exercise (e.g., Yang et al., 1985; Rosenbloom & Anderson, 1994); however, by using high-resolution DEMs and mathematical models, knickpoints can be identified using slope-area relationships and stream gradient calculations (e.g., Bishop et al., 2005; Hayakawa & Oguchi, 2006, 2009; Howard & Kerby, 1983).

3. Numerical Model for the Formation of Multiscarps

Numerical models of fault scarp diffusion have been used to explore the degradation of composite fault scarps (Avouac & Peltzer, 1993) on the assumption that erosion is transport limited as would be the case for soil-mantled landscapes (Arrowsmith et al., 1998). However, the morphological changes caused by the degradation of multiscarps is less well known. Here, we illustrate how the interplay between coseismic surface offsets and degradation causes the formation of multiscarps using a numerical solution to the one-dimensional diffusion equation (e.g., Andrews & Hanks, 1985; Arrowsmith et al., 1998; Culling, 1963; Hanks et al., 1984; Nash, 1980), which calculates changes in elevation Z along a scarp profile (where x is the horizontal distance) over time t (Figure 2). Assuming the scarp erosion is transport limited (where more debris is available for removal than processes are capable of removing), the vertical component of

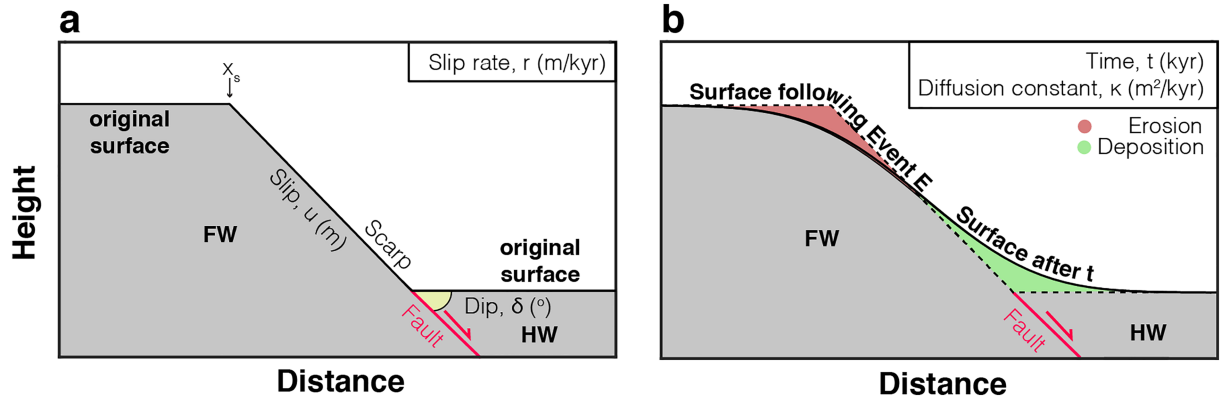

Figure 2. Scarp degradation model for soil-mantled fault scarps. (a) Parameters used to generate a catalog of synthetic fault scarps. FW = footwall; HW = hanging wall. (b) Parameters used for the degradation of a fault scarp profile using a one-dimensional diffusion equation.

scarp degradation is governed by the conservation of mass and can be applied using the equation (Smith & Bretherton, 1972):

$$\frac{dZ}{dt} = \kappa \frac{d^2 Z}{dx^2} \tag{1}$$

where κ is the diffusion constant (m^2/Kyr). Scarp degradation processes transport material from the crest of the fault scarp and deposit it at the base of the scarp, smoothing the scarp and reducing the average slope below the fault dip angle δ (Figure 2b). As the mechanical properties of bedrock are not considered by this equation, it is only strictly applicable to soil-mantled fault scarps.

In our model, an initial scarp is generated at distance x_s along the profile assuming a down-dip, normal sense of displacement on a fault with dip δ, following an earthquake of slip u (Figure 2a). We assume an even slip distribution on the fault, including the surface offset and assume that the slope of the scarp and dip of the fault are equal following the rupture. By dividing the slip by the fault slip rate r, the time between ruptures T_R can be found (also known as the recurrence interval or return period). Between earthquakes, the scarp is degraded according to equation (1), and we chose a diffusion constant, κ, in the range of 5–10 m^2/Kyr suitable for subtropical climates. This lies between values proposed for semiarid climates (0.5–5 m^2/Kyr; e.g., Andrews & Hanks, 1985; Arrowsmith et al., 1996; Carretier et al., 2002; Hanks et al., 1984; Kokkalas & Koukouvelas, 2005; Niviére & Marquis, 2000) and tropical climates (Zielke & Strecker, 2009; e.g., 10 m^2/Kyr). Estimates for κ may also be affected by vegetation (Hanks et al., 1984). As expected, a larger diffusion constant κ causes more erosion and decreases the slope of the scarp.

The model simulation is run over a fixed period of time T, for a certain number of events. For multiple ruptures, model parameters (u, r, δ, x_s, etc.) may be fixed for the entire simulation period or varied per event. For the fixed parameter scenario, a fault scarp caused by a single rupture and a composite fault scarp generated by three smaller ruptures (on the same fault plane) both degraded to identical profiles after a certain diffusion age (Figures 3a and 3b). For a 60° dipping normal fault, the transition from composite scarps to degraded scarp (i.e., when clear slope break points were removed) occurred at $\kappa t \sim 36$ m^2. For a 40° fault, the transition occurred at $\kappa t \sim 20$ m^2. For κ in the range of 5 and 10 m^2/Kyr, this corresponds to a minimum of 2,000 years to create degraded scarps from composite scarps. Of course, this also depends on many factors that may have localized influences such as lithology, geological discontinuities (e.g., joints), and moisture content.

Multiscarps formed during variable parameter simulations which considered decreases in fault dip of >10° per earthquake and changes to the active fault location, that is, the formation of splays (Figures 3c–3f). Moving the active fault plane toward the lower original surface created an asymmetric slope profile with a smoother tail toward the scarp top (Figure 3d), whereas the opposite was observed when the active fault was moved toward the upper original surface (Figure 3e). By alternating the active fault plane between two parallel surfaces, two composite scarps separated by a break in slope (i.e., a hybrid composite multiscarp) may develop (Figure 3f). The length between the base of one scarp and the crest of another was slightly smaller than the distance between faults due to the degradation of two scarp surfaces that the terrace separates.

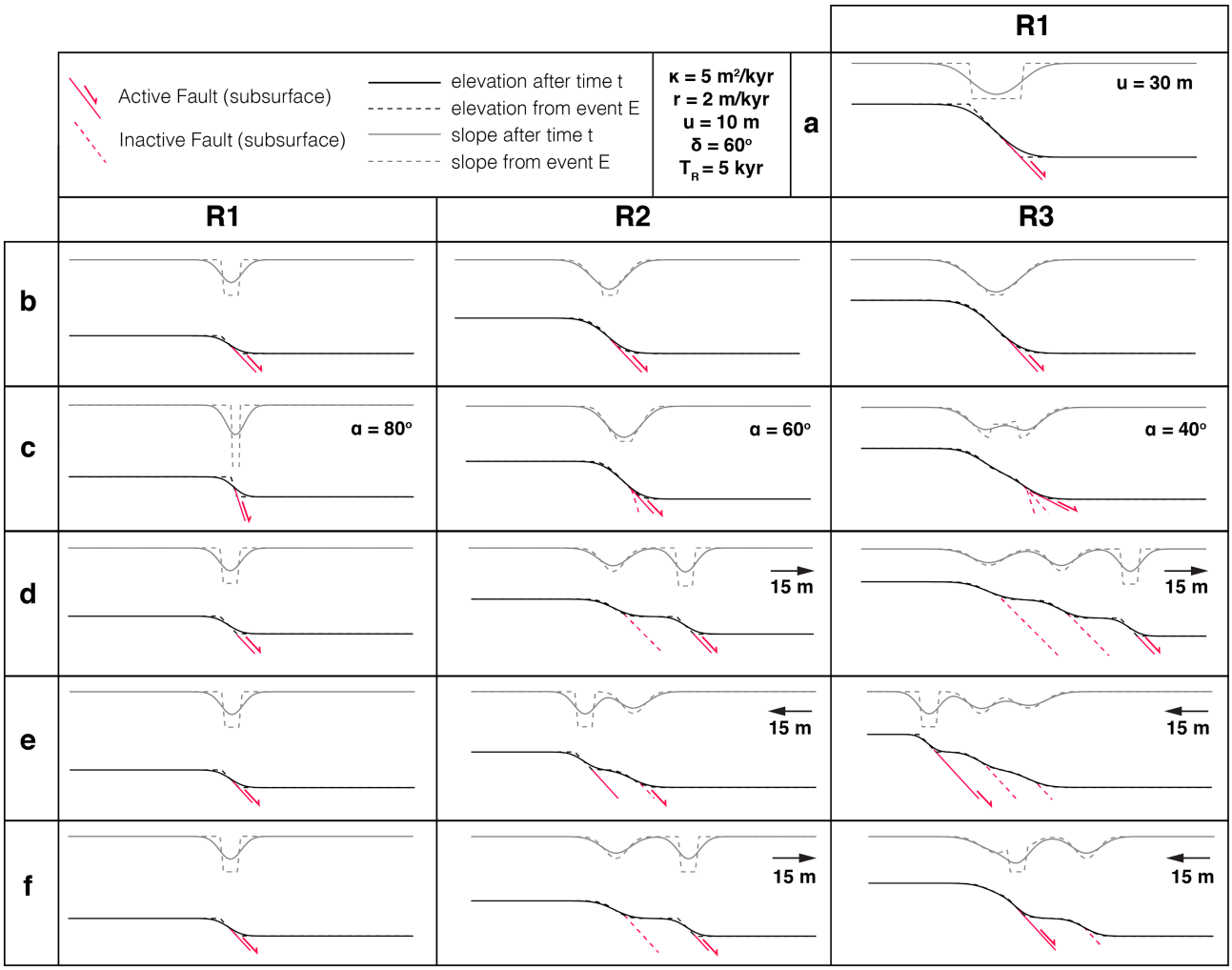

Figure 3. The synthetic fault scarp formation and degradation. (a) A single rupture scarp. (b) A composite scarp formed by three equally sized ruptures (R1–R3). (c)–(f) Multiscarps formed by (c) decreases in fault dip δ per rupture, (d) movement of the active fault plane (solid red line) into the hanging wall, (e) movement of the active fault plane into the footwall, and (f) alternating the active fault between two fault planes. The dashed lines denote the elevation (black) and slope (gray) profiles immediately following the rupture. The solid lines denote the profiles at the end of the recurrence interval T_R.

These model results illustrate how degraded multiscarp and composite scarps have a different morphological expression (Figure 3). This provides a theoretical framework in which normal fault multiscarps can be interpreted, and we now move to an analysis of such scarps in a natural setting.

4. Data Acquisition and Processing

4.1. Tectonic Setting of the BMF

The Malawi Rift is a 900 km long amagmatic section of the Western Branch of the East African Rift System (EARS; Ebinger et al., 1987, 1989). It consists of a series of ~100–150 km long grabens and half grabens, which are defined by basin bounding faults (Ebinger et al., 1987; Flannery & Rosendahl, 1990; Laó-Dávila et al., 2015). The northern and central parts of the Malawi Rift have been flooded by Lake Malawi; however, its three southernmost grabens are still exposed onshore (Dulanya, 2017; Hodge et al., 2019). Based on EARS-scale kinematic models, the Malawi Rift is currently accommodating ~2 mm/year east-west extension for a fixed Nubian Plate reference frame (Saria et al., 2014; Stamps et al., 2018).

The BMF lies within the Makankijra Graben and extends for 110 km from the southern end of Lake Malawi to the northern end of the Zomba Graben (Figure 4a). The BMF is slightly oblique to the current extension direction but is considered to be pure normal as (1) no strike-slip offsets have been observed in the field or in DEMs (Hodge et al., 2018a) and (2) it is broadly parallel to the structure that may have been the source

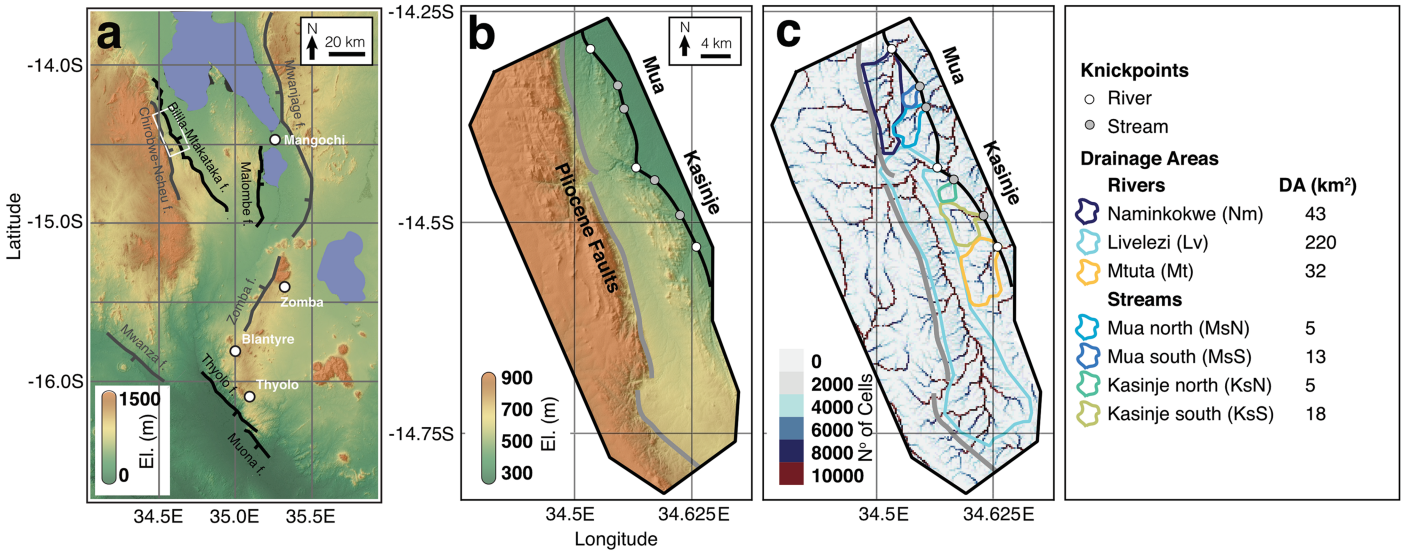

Figure 4. (a) Overview map of Makanjira graben, south Malawi. The Mua and Kasinje segments are shown by the white box on the Bilila-Mtakataka fault. (b) The 30 m SRTM DEM and hillshade for the Mua and Kasinje segments, showing the location of where the major rivers cross the scarp (identified in the field). (c) The number of cells that drain through each cell, that is, the discharge capacity, with the inferred drainage basins represented by polygons. Drainage area is also given in km^2.

of the 1989 Salima earthquake, which had a rake of −92° ± 25° and an epicenter 40 km north of the BMF's surface expression (Jackson & Blenkinsop, 1993). This apparent dichotomy between its normal kinematics and slight obliquity to the regional extension direction can be explained by the presence of a deep-seated crustal weakness (Hodge et al., 2018b; Philippon et al., 2015), consistent with structural analysis that shows normal faults with a range of orientations can be reactivated within a uniform stress field (Williams et al., 2019).

The BMF juxtaposes amphibolite-grade Proterozoic gneisses and granulites in the footwall against post-Miocene sediments in the hanging wall (Dulanya, 2017; Hodge et al., 2018b; Jackson & Blenkinsop, 1997; Walshaw, 1965). The landscape is soil mantled, albeit with some rocky outcrops (Figures 5a and 5b). In contrast, river channels are rocky with little sediment remaining in the channels (Figures 5c and 5d). This is consistent with the standard assumptions for the geomorphological analyses performed here, namely, that (1) degradation of the scarp is transport-limited and (2) retreat of the knickpoints is detachment limited (Arrowsmith et al., 1998; Whipple & Tucker, 1999).

4.2. Data Processing

To determine whether the BMF scarp records multiple earthquake events, as is qualitatively observed (Figure 6), we use a submeter point cloud generated from Pleiades imagery (Hodge et al., 2019). Because of the size of the point cloud (in excess of 30 GB), to save computational resources, we restrict our study area to the two major segments at the centre of the BMF: the Mua and Kasinje segments (Figures 4b and S1) that are found to contain the largest scarps (>20 m high) along the entire fault (Hodge et al., 2019, 2018b). Both the average height of these segments and the average scarp height (used as a proxy for vertical displacement; e.g., Morewood & Roberts, 2001) along the entire fault (~14 m) exceed the magnitude of slip typical of a single event for a fault the length of the BMF (<10 m; Scholz, 2002). Therefore, due to this and their central location along the BMF, the Mua and Kasinje segments may be the most likely segments to show evidence of multiple ruptures at the surface.

The BMF scarp is soil mantled and the area surrounding it is densely vegetated (Figures 4b, 5a, 5b, 6, and S1), which causes significant, local fluctuations in elevation data (Hodge et al., 2019). When this noise propagates into slope calculations, it affects scarp parameter calculations, and so to analyze the submeter point cloud used in this study, we first improve the signal-to-noise ratio. To mask vegetation, a normalized difference vegetation index (NDVI) is calculated from the red (R) and near-infrared (NIR) bands (e.g., Elvidge & Lyon,

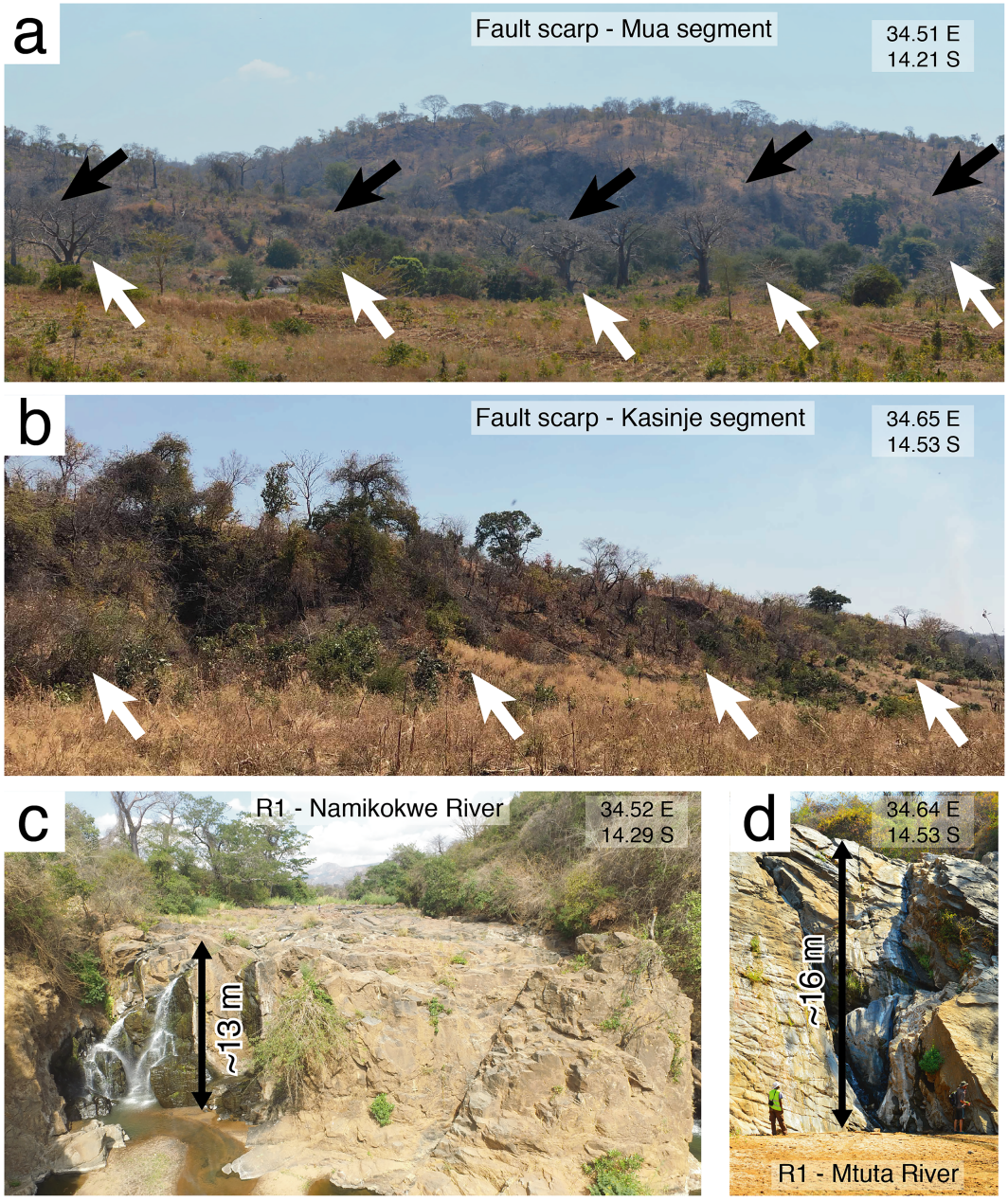

Figure 5. Field photos of the Bilila-Mtakataka fault scarp (a,b) and knickpoints (c,d). (a) Fault scarp along the Mua segment. (b) Fault scarp along the Kasinge segment. White arrows indicate the base of the scarp and black arrows the top of the scarp. The scarps are soil mantled, with occasional rocky outcrops, consistent with the behavior of hillslopes (and thus fault scarps) that erode in a diffusive manner. (c) Knickpoint R1 along the Namikokwe River. (d) Knickpoint R1 along the Mtuta River. The height of each knickpoint was estimated using photo analysis and corresponds well with the R1 knickpoint heights extracted from the Pleiades imagery (Figures 10 and 11). The rocky river channels shown here suggest that the retreat of these knickpoints is a detachment limited process.

1985; Grigillo et al., 2012; Rawat & Joshi, 2012; Yu et al., 2011):

$$NDVI = \frac{NIR - R}{NIR + R}. \quad (2)$$

For 50 representative sample points, the median NDVI value for vegetated and nonvegetated areas was found to be 0.57 and 0.33, respectively (Figure S1). Nonvegetated areas were also found to have a larger composite RGB value than vegetated areas (i.e., they are lighter in RGB color). The best performing NDVI threshold to reflect the transition to vegetation was 0.45, where just 4% of sample points were incorrectly identified

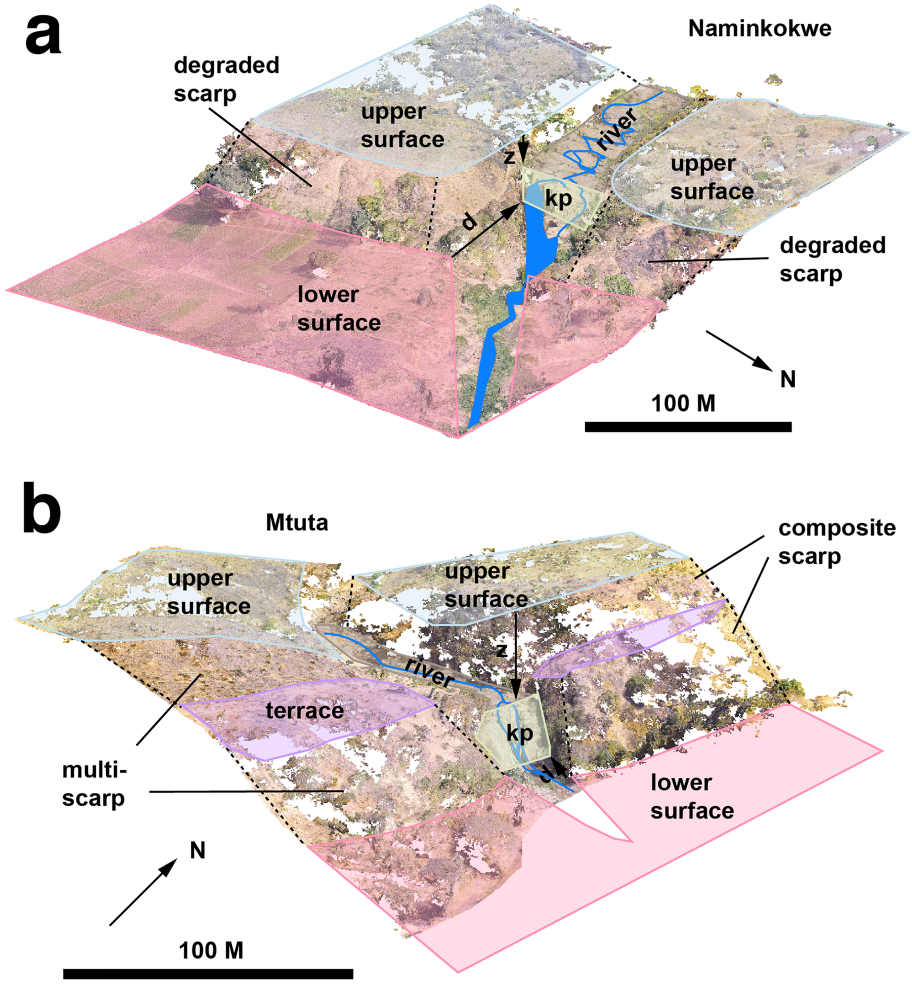

Figure 6. Oblique views of the Bilila-Mtakataka fault scarp from a drone-based digital elevation model. (a) Naminkokwe River (Mua segment) and (b) Mtuta River (Kasinje segment). These images show local evidence for composite scarps and multiscarps. Knickpoints (kp) are clearly visible in both rivers.

($n = 100$; Figure S1). Note that this is higher than previous studies which have reported that a NDVI value greater than 0.2 coincides with vegetation coverage (Grigillo et al., 2012). However, this difference may be due to differences in camera calibration and color levels. In addition, we manually remove additional large-scale noise features such as buildings that cannot be captured using the NDVI method.

4.3. Scarp Profiles

Twenty-one scarp profiles along the Mua segment and 18 from the Kasinje segment were identified as having a sufficient point cloud density (>90% coverage and no gaps > 10 m) to be analyzed (Figure S1). To account for geometrical variations along the segments influencing our vertical displacement calculations (e.g., Mackenzie & Elliott, 2017), profiles were oriented to perpendicular to the average trend of the BMF (150°) Hodge et al. (2018b). For each profile, points were taken at intervals of a half meter. The minimum scarp profile length is 300 m.

Despite improving the signal-to-noise ratio, we find that local noise still results in variations in the gradient with an amplitude comparable to that expected by a scarp or knickpoint. To further improve the signal-to-noise ratio, we apply a digital filter to the elevation profiles. We use the *rloess* function in MATLAB as a filter, which is a more robust version of the Loess filter (Cleveland, 1981). The quadratic regression used by *rloess* is more computationally expensive than the Loess filter but is better at removing outliers while not without drastically influencing the elevation or slope profiles (Hodge et al., 2019). As we do not want to artificially reduce the scarp slope or smooth over slope breaks, we choose a bin width of 15 m. Smaller window sizes failed to successfully eliminate background noise close to scarps.

4.4. River Profiles

The rocky character of the rivers and streams in this area (Figures 5c and 5d) suggests knickpoint positions and retreat rates may encode information about the downstream fault's tectonic history. The geological map by Dawson and Kirkpatrick (1968) shows the Naminkokwe River as the only major river that crosses the BMF scarp, but during fieldwork, we identified two additional rivers that are suitable for knickpoint analysis: the Livelezi and Mtuta rivers (white circles Figure 4b). The Naminkokwe River is located at the northern end of the Mua segment (~37 km from the northern end of the fault). It is ~10 m wide on average, including where it crossed the fault scarp, but has a prominent 20 to 30 m wide section between 50 and 200 m from the scarp. The Livelezi River, which is located at the intersection between the Mua and Kasinje segments (near the town of Golomoti), is reasonably well-defined where it crosses onto the valley floor, comprising a width of around 20 m. Upstream the river is locally up to 100 m wide but averages ~30 m. The larger channel width of the Livelezi River compared to the Naminkokwe River suggests it has a larger flow discharge (Leopold & Maddock, 1953). The Mtuta River has a maximum width of ~10 m but had significantly less discharge passing through it than the other rivers observed during fieldwork in the dry season. We identified four smaller unnamed channels using the DEM, and since these are <5 m wide, we refer to them as streams and label them according to their location within the segment: Mua north, Mua South, Kasinje North, and Kasinje South (gray circles; Figure 4b). During the fieldwork, no discharge passed through each stream. How discharge changes during the wet season for each river and stream is unknown to us currently.

Each channel was traced from the Pleiades point cloud using the polyline tool in CloudCompare®. The nearest point from the Pleiades point cloud to the polyline was selected within a parallel distance of 2 m, at an interval of a half meter. The extracted point cloud was manually cleaned to remove noise. Because of smaller channel widths, the streams had more noise due to overhanging vegetation from the channel sides. This resulted in significant gaps in the extracted profiles for some streams. The points were then plotted along the length of the detailed channel, to form a two-dimensional profile where the horizontal axis is the distance from the fault scarp. As a smoothed longitudinal profile also better represents the true channel bottom (Wei et al., 2015), we apply a digital filter to improve the signal-to-noise ratio. As we want to preserve the vertical to subvertical gradients of the knickpoints to identify them in the river profiles, we use a Savitzky-Golay filter, which is based on local least squares polynomial approximation (Savitzky & Golay, 1964) and helps preserve data features such as peak height and width. Due to the large elevation artifacts of the noise on the channels, we set the window size to be 20 m. Although all the channels show a clear downslope trend, there are sections that show a small, localized upslope trend, which is likely the result of vertical or horizontal uncertainty. The vertical uncertainty may be a few meters, especially where parts of the scarp are far away from ground control points used to develop the DEM from the stereo-pair. Similarly, our polyline may not follow the true channel, for example, if there is a lower section adjacent to the selected point or there is overhanging vegetation cover that was not removed by the filter. However, these minor upslope trends could also be real and may be overcome by the increased channel flow velocity and height during the wet season.

River drainage area is considered to be an important factor in the speed at which a knickpoint retreats through a river system (e.g., Berlin & Anderson, 2007; Bishop et al., 2005; Crosby & Whipple, 2006; Hayakawa & Oguchi, 2006; Seidl et al., 1994). We performed a hydrological analysis on a 30 m SRTM DEM in QGIS (Figure 4b) to compute drainage direction and discharge capacity (Figure 4c). A polygon was then drawn around the tributaries that drained into each river or stream at the point they incised the scarp to reflect the estimated drainage area (Figure 4c). As we are not certain of the hydrological processes acting over the Chirobwe-Ncheu fault to the west and whether discharge flows over this fault and into the rivers or streams in this study, our polygons do not extend into the footwall of this fault. The results show that the Livelezi River has a drainage area in excess of 200 km^2, the Naminkokwe and Mtuta Rivers have drainage areas of 43 and 32 km^2, respectively, and the four smaller streams have drainage areas <20 km^2.

5. Fault Scarps

5.1. Scarp Analysis Methods

Using the characteristics typical of single or multiple surface ruptures on fault scarps (Figure 1), we categorize each profile as either (i) a single rupture scarp, (ii) a degraded scarp, (iii) a composite scarp, or (iv) a multiscarp. Scarp surfaces are marked by steep gradients and troughs in the calculated slope profile. Slope breaks are marked by gentle gradients separating multiple troughs. For composite scarps, the number of

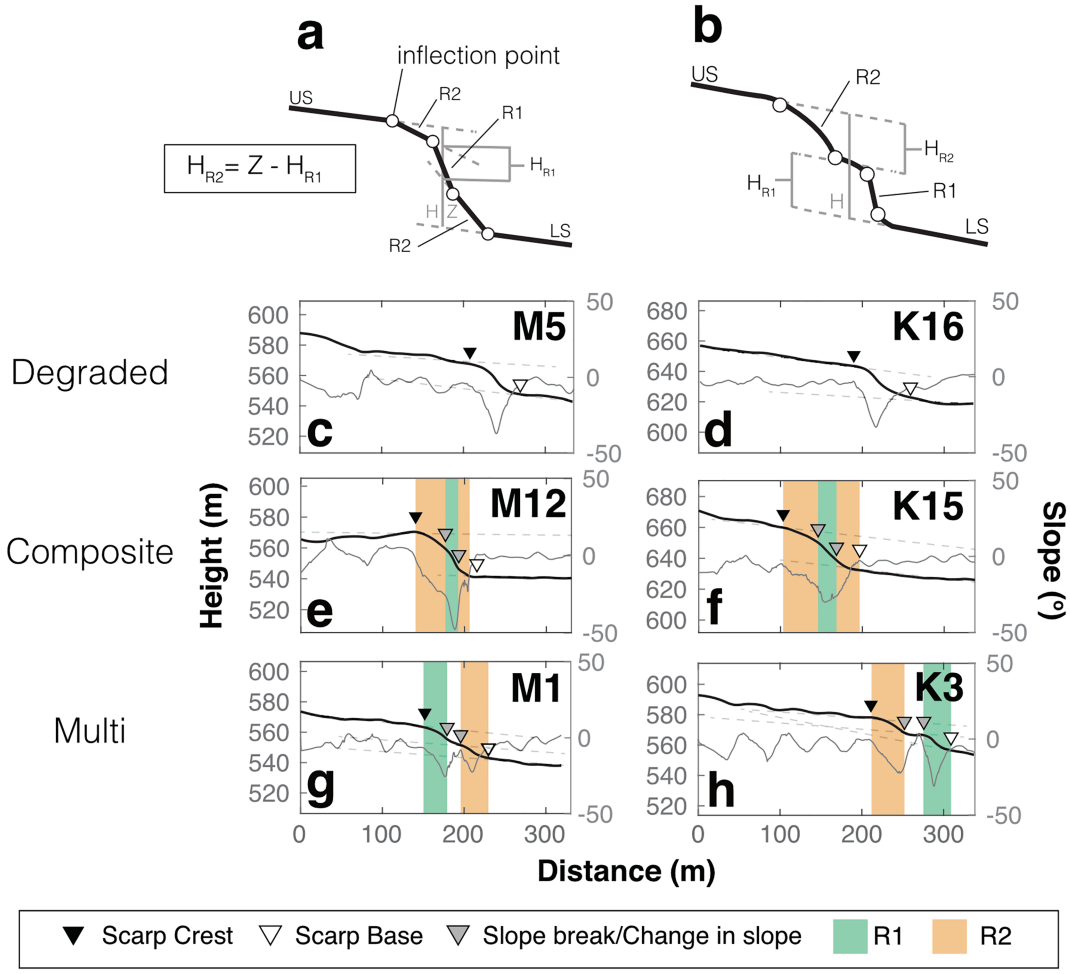

Figure 7. Schematic showing (a) composite scarp and (b) multiscarp profile. (a) The scarp height of the most recent rupture event R1 (H_{R1}) is calculated by fitting a regression line to the R2 rupture surfaces and calculating the elevation difference at the location corresponding to the maximum slope on the R1 scarp surface. The scarp height of a subsequent rupture event (i.e., H_{R2}) is then found by calculating the elevation difference (Z) using the regression line approach and the next older rupture surface, or original surfaces if calculating the oldest rupture, and subtracting the cumulative scarp heights of earlier ruptures (i.e., H_{R1}). (b) Regression lines are fitted to the upper (US) and lower (LS) original surfaces and the terraced surface (slope break) between scarps. The scarp height for each rupture event is then calculated as the elevation difference between regression lines at the slope maxima. (c–h) Three examples from the Mua (c,e,g) and Kasinje segments (d,f,h): a degraded scarp with no indicators of multiple ruptures (c,d), a composite scarp with multiple events (e,f), and a multiscarp with multiple rupture events (g,h). Filled black triangles denote the crest of the entire fault scarp. Filled white triangles denote the scarp base. Filled gray triangles denote breaks or changes in slope between individual scarp surfaces formed by multiple ruptures. The steepest surfaces corresponding to R1 are colored green, and the gentler surfaces corresponding to R2 are colored orange.

ruptures is quantified by the number of slope changes (i.e., pairs of major slope break points), and for multiscarps, the number of slope breaks. We note that degraded scarps may be fault scarps that have experienced multiple ruptures but have undergone sufficient degradation for individual rupture markers to be lost (e.g., Bucknam & Anderson, 1979; Nash, 1984; Wallace, 1980). As a result, for all scarp types, the number of ruptures is a minimum estimate.

The total scarp height H for each profile was calculated as the cumulative surface displacement along the fault (Figures 7a and 7b; Hodge et al., 2018b). First, the crest and base of the entire scarp (regardless of whether it contains multiple rupture indicators) were picked manually, then a regression line was fitted to the upper and lower original slopes. The scarp height is then calculated as the difference between the two regression lines at a location corresponding to the maximum slope on the scarp surface.

For multiscarp profiles, the crest and base of each individual scarp surface (identified by breaks in slope) were manually picked and the scarp height of each calculated using the regression line method (Figure 7b). As scarps smooth over time due to degradation (e.g., Bucknam & Anderson, 1979; Nash, 1984; Wallace, 1980) and as the lithology along both segments is uniform at fault scale (Hodge et al., 2018b; Walshaw, 1965) implying limited spatial variability in diffusivity, we order the scarp surfaces in terms of slope steepness, from steepest to gentlest. We then infer the steepest surface to be a less degraded, younger scarp surface and hence represent the most recent rupture event (R1), the next steepest surface to represent the next most recent rupture event (R2), and so forth. We note that the most recent surface rupture here denotes the most recent "observable" surface rupture, where a more recent surface rupture may have occurred but may have been too small to identify or eroded away. The horizontal distance between scarp surfaces (i.e., between one scarp surfaces base and another's crest) was also measured for multiscarps.

For composite scarps, the scarp height of R1 (H_{R1})—identified as the steepest scarp surface at the center of the scarp—was calculated by fitting a regression line to the R2 surfaces and calculating the elevation difference at the location corresponding to the maximum slope on the R1 scarp surface (Figure 7a). The scarp height of earlier rupture events are then found by calculating the elevation difference (Z) using the regression line approach and the next older rupture surface, or original surfaces if calculating the oldest rupture, and subtracting the cumulative scarp heights of subsequent ruptures, that is, $H_{Rn} = Z - \sum_{i=1}^{n-1} H_{Ri}$.

5.2. Results of Scarp Analysis

The average total scarp height for all profiles was 22 ± 5 m; the average total scarp height for Mua profiles was slightly smaller (21 m) than Kasinje (22 m) but had a smaller standard deviation (6 m compared to 7 m; Figure 8c). On average, the total scarp height is larger at the center of the segments than the edges, as has been previously observed (Hodge et al., 2019, 2018b). For several kilometers toward the intersegment zone (Livelezi River), the total scarp height for both segments decreases by up to 15 m; however, the local scarp height near the river increases by up to 10 m on both segments.

Figures 7c–7h show examples of degraded and composite scarps and multiscarps from the Mua and Kasinje segments. As no free faces were identified on any profile, none were categorized as a single rupture scarp (i.e., fresh scarp that formed in the last few decades). Profiles M5 and K16 are examples of degraded fault scarps, displaying a smooth elevation profile and symmetrical slope profile. M12 and K15 however show an increase in slope toward the scarp center (highlighted green in Figures 7e and 7f), typical of a recent rupture on a preexisting scarp; these profiles are interpreted as composite scarps. Breaks in slope typical of multiscarps can be found on M1 and K3, where the steepest scarp surface is shown in green in Figures 7g and 7h.

Out of the 39 profiles, 19 were categorized as degraded scarps (9 on Mua and 10 on Kasinje), 14 as composite scarps (nine on Mua and five on Kasinje), and six as multiscarps (three on both Mua and Kasinje). For multiscarps, the steepest scarp surface (R1) was nearest the lower original surface for all but one profile (M1). For the 20 profiles where multiple events could be identified (i.e., composite scarps or multiscarps), all but one showed evidence for two subscarps (R1 and R2; Figure 8b). The anomalous result, multiscarp profile K12, has an additional break in slope (R3).

Our numerical model demonstrated that multiscarps are formed by fault splays (Figures 3d–3f), which is consistent with rupture of anisotropic rocks leading to the activation of different surfaces (e.g., Hodge et al., 2018b; Lee et al., 2002). Here, the majority of the multiscarps on the two BMF segments were recorded at segment tips. This is consistent with fault splay formation at segment tips observed in other natural examples (Giba et al., 2012; Manighetti et al., 2001; Segall & Pollard, 1983; Wu & Bruhn, 1994), as well as experiments and theoretical models (Perrin et al., 2016a, 2016b; Willemse & Pollard, 1998).

For the degraded scarps, the average scarp heights were 21 ± 5 and 22 ± 5 m, respectively, for Mua and Kasinje. The total scarp heights for composite scarps and multiscarps were ~23 m for both segments and therefore comparable to the average height of the degraded scarps. For composite scarps and multiscarps, the scarp height of R1 was on average 11 ± 2 m for the Mua segment and 13 ± 4 m for the Kasinje segment (green symbols, Figure 8a). For the Mua segment, the R1 scarp height was fairly constant, whereas it was more variable on the Kasinje segment and increased southward. The scarp related to R2 (orange symbols, Figure 8a) had a height of 12 ± 4 and 10 ± 4 m for Mua and Kasinje, respectively. The scarp height of R2

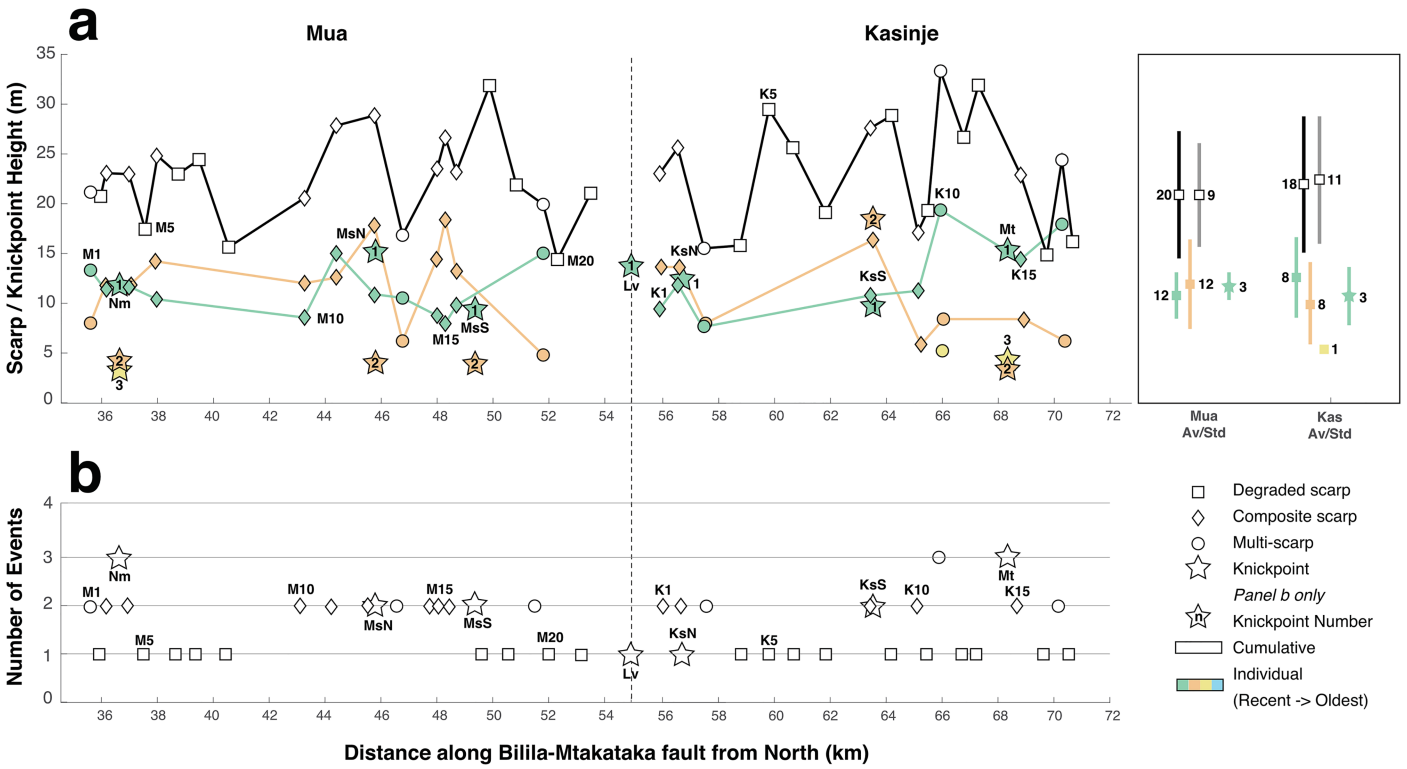

Figure 8. (a) The total scarp height for scarp profiles (white filled), against individual scarp heights for the last rupture event (R1, green), penultimate rupture event (R2, orange), and third rupture event (R3, yellow), for scarp analyses. The box at the end of the profile shows the average (squares) and standard deviation (error bars) values for the scarp height of the following: total (black), degraded (gray), R1 (green), R2 (orange), and R3 (yellow). Knickpoint results are shown as stars corresponding to the inferred rupture event. (b) The number of rupture events inferred from the scarp profiles (square = degraded scarps, diamond = composite scarps, circle = multiscarps) and knickpoints (stars) for the Mua and Kasinje segments.

is greatest at the center of the segments. A third subscarp (R3) on Profile K12 was identified, comprising a scarp 5 m high.

5.3. Estimating Diffusion Age

Previous studies have applied the scarp degradation model shown in Figure 2 to natural fault scarps in soil-mantled landscapes. Using the slip and slip rate along a fault to estimate the date of the scarp-forming earthquake or earthquakes, it is possible to calculate the diffusion constant κ (e.g., Arrowsmith et al., 1998; Avouac & Peltzer, 1993; Carretier et al., 2002). For the BMF, neither the date of past earthquakes nor the slip rate is known, so we cannot directly estimate the diffusion constant κ. Instead, we estimate the diffusion age κt (i.e., the amount of erosion that has occurred on the scarp since the earliest earthquake). Note that the term diffusion age is widely used in the literature but is misleading as it actually corresponds to the area given by the product of diffusivity κ and chronological age t (Andrews & Hanks, 1985). By making some assumptions about κ, we may then be able to convert κt to find the relative differences in age between scarp profiles.

We estimate the age of the 33 composite or degraded scarp profiles along the Mua and Kasinje segments shown in Figure 8a. As the negative change in elevation at the upper portion of the scarp should correspond to an equal positive change in elevation at the bottom of the scarp, only the erosion at the upper scarp needs to be calculated. First, the intersection is found between a regression line fitted to the upper surface and one fitted to the scarp surface. The two regression lines are then joined to reproduce the original scarp surface before degradation. Using equation (1), the initial scarp is degraded over a period of time of T at intervals of t. We assume a fault dip of 60° in the absence of other information. At each step, the goodness of fit is assessed by comparing the modeled scarp profile against the observed scarp profile by estimating the root mean square error (RMSE). Confidence intervals are defined by considering profiles within a 5 cm range of $RMSE_{min}$ (Arrowsmith et al., 1998; Avouac & Peltzer, 1993).

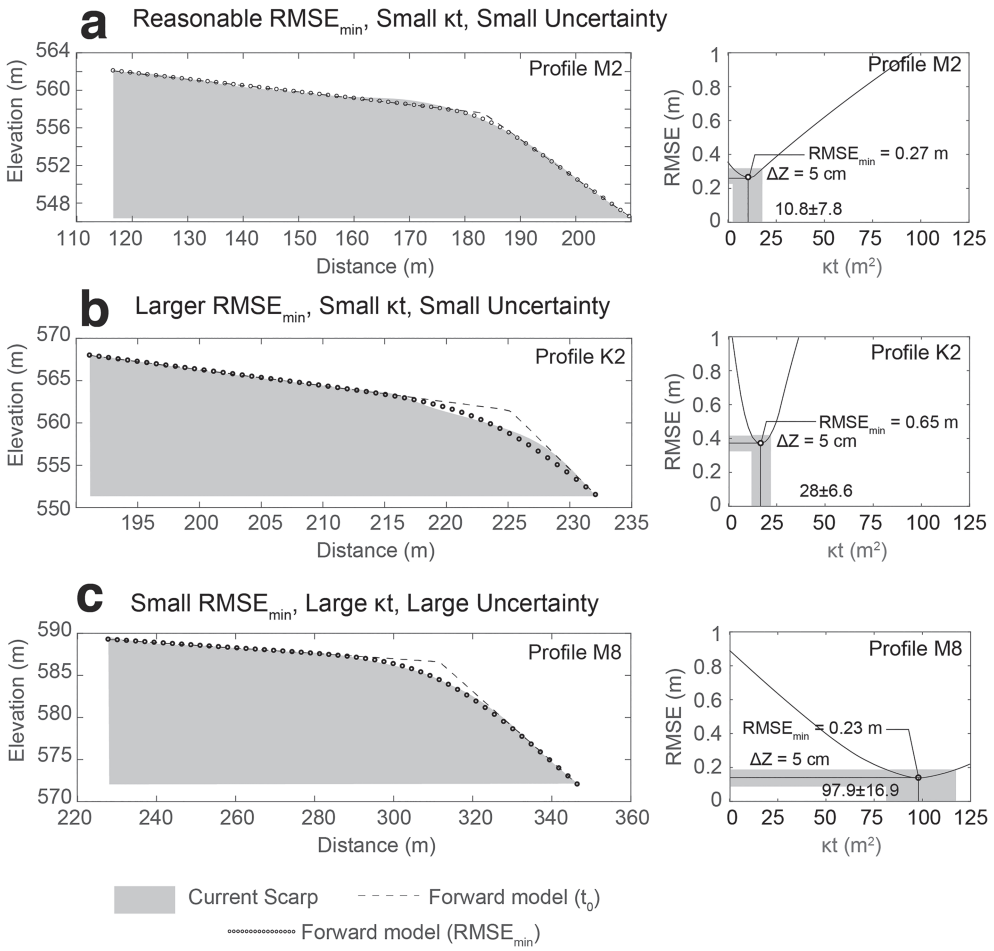

Figure 9. Diffusion age (κt) calculations for three selected examples: (a) Profile M2 where a reasonable $RMSE_{min}$ (0.27) was found for a κt of 11 ± 8 m^2, (b) Profile K2 where a large $RMSE_{min}$ (0.65) was found for a κt of 28 ± 7 m^2, and (c) Profile M8 whose $RMSE_{min}$ of 0.23 shows a good model fit to a κt of 98 ± 17 m^2.

The average diffusion age for the 33 scarp profiles is 48 ± 25 m^2 with a range of ~1 to 98 m^2. Minimum misfit ($RMSE_{min}$) between forward model and observations varies from less than 0.1 m (e.g., Profiles M3, M17, K5, and K13) to ~1 m (Profile M9), with an average of ~0.2 m. Profile M2 is an example of a reasonably well-fitting profile ($RMSE_{min}$ 0.3 m) for a small diffusion age (11 ± 8 m^2; Figure 9a). In comparison, Profile K2 was estimated to have a similarly low diffusion age (16 ± 5 m^2), but the model fit was worse ($RMSE_{min}$ 0.4 m; Figure 9b). The poor fit for Profile K2 is due to the variable scarp slope near the scarp crest, a feature typical of composite scarps. In comparison, Profile M2 is a degraded scarp and therefore has a smoother slope profile. Profile M8 is an example of a scarp that has a large estimated diffusion age (98 ± 17 m^2), where the fit between the model and observations were good but uncertainty was large ($RMSE_{min}$ 0.1 m; Figure 9c). The inverse solution of the model estimated a κt of just ~1 m^2 for Profile M9, but the $RMSE_{min}$ was ~1 m, indicating a very poor fit.

The average diffusion age for the 33 scarp profiles is 48 ± 25 m^2 with a range of ~1 to 98 m^2. Minimum misfit ($RMSE_{min}$) between forward model and observations varies from less than 0.1 m (e.g., Profiles M3, M17, K5, and K13) to ~1 m (Profile M9), with an average of ~0.2 m. Profile M2 is an example of a reasonably well-fitting profile ($RMSE_{min}$ 0.3 m) for a small diffusion age (11 ± 8 m^2; Figure 9a). In comparison, Profile K2 was estimated to have a similarly low diffusion age (16 ± 5 m^2), but the model fit was worse ($RMSE_{min}$ 0.4 m; Figure 9b). The poor fit for Profile K2 is due to the variable scarp slope near the scarp crest, a feature typical of composite scarps. In comparison, Profile M2 is a degraded scarp and therefore has a smoother slope profile. Profile M8 is an example of a scarp that has a large estimated diffusion age (98 ± 17 m^2), where the fit between the model and observations were good but uncertainty was large ($RMSE_{min}$ 0.1 m; Figure

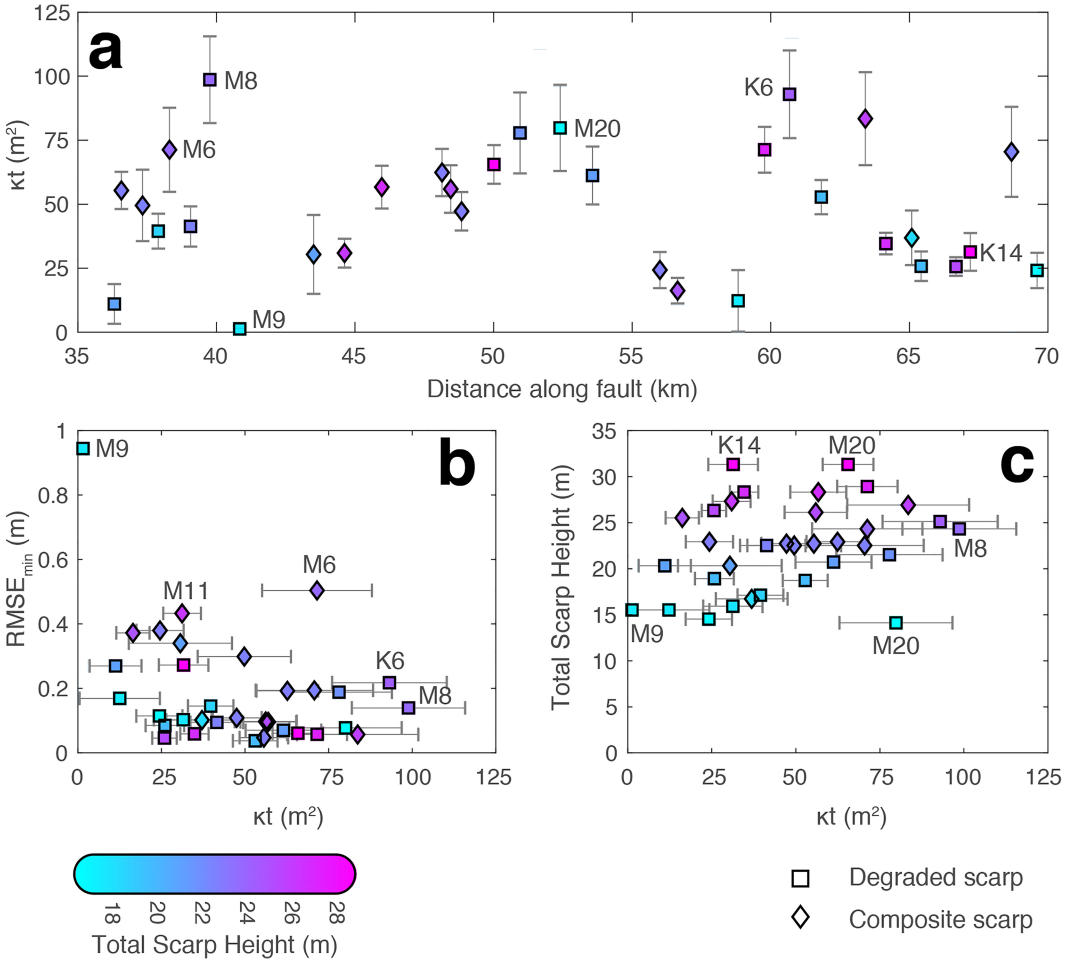

Figure 10. Diffusion ages κt for scarp profiles across the Mua and Kasinje segments of the Bilila-Mtakataka fault. (a) The estimated κt plotted against the distance along the fault; (b) RMSEmin versus κt, and (c) total scarp height versus κt.

9c). The inverse solution of the model estimated a κt of just ~1 m^2 for Profile M9, but the RMSE$_{min}$ was ~1 m, indicating a very poor fit.

In general, a better model fit was found for scarps with a larger diffusion age (Figure 10b). Of the 18 profiles whose κt is estimated to be less than 50 m^2, six have a RMSE$_{min}$ of 0.3 m or greater (M4, M9, M10, M11, K1, and K2), whereas only one profile has an equivalent RMSE$_{min}$ where κt is >50 m^2 (M6). Smaller scarps typically have a smaller κt than larger scarps (Figure 10c). The smallest scarp (K16, ~15 m high) has a κt of ~24 ± 7 m^2, whereas the largest scarp (M17, ~31 m high) has a κt of ~65 ± 8 m^2. Profile M20 is the anomalous result to this relationship, where an ~14 m high scarp has a κt of 80 ± 17 m^2. This scarp is located within 5 km of the intersegment zone. Typically, Mua segment scarps close to the intersegment zone have larger estimated κt values than those at comparable distances on the Kasinje segment (Figure 10a).

The Mua and Kasinje segments have the same average κt value within error (Figure 10). The estimated κt value for the Mua segment is 52 ± 24 m^2 (n = 18) and for the Kasinje segment is 42 ± 26 m^2 (n = 15). For both segments, degraded and composite scarps have a similar average diffusion age (~50 m^2), but degraded scarps have a larger standard deviation. This may imply that there is no major difference in diffusion (or age) between the two types of scarps. Profiles M8 and K6 have the largest estimated diffusion age (95 ± 20 m^2) and M2 and K4 the smallest (11 ± 0 m^2; Figure 10a). This is likely due to the steep surface near the scarp crest, which the model could not fit a reasonable degraded surface to. Typically, κt values are lower at the segment ends than the center, but variations do occur (Figure 10a).

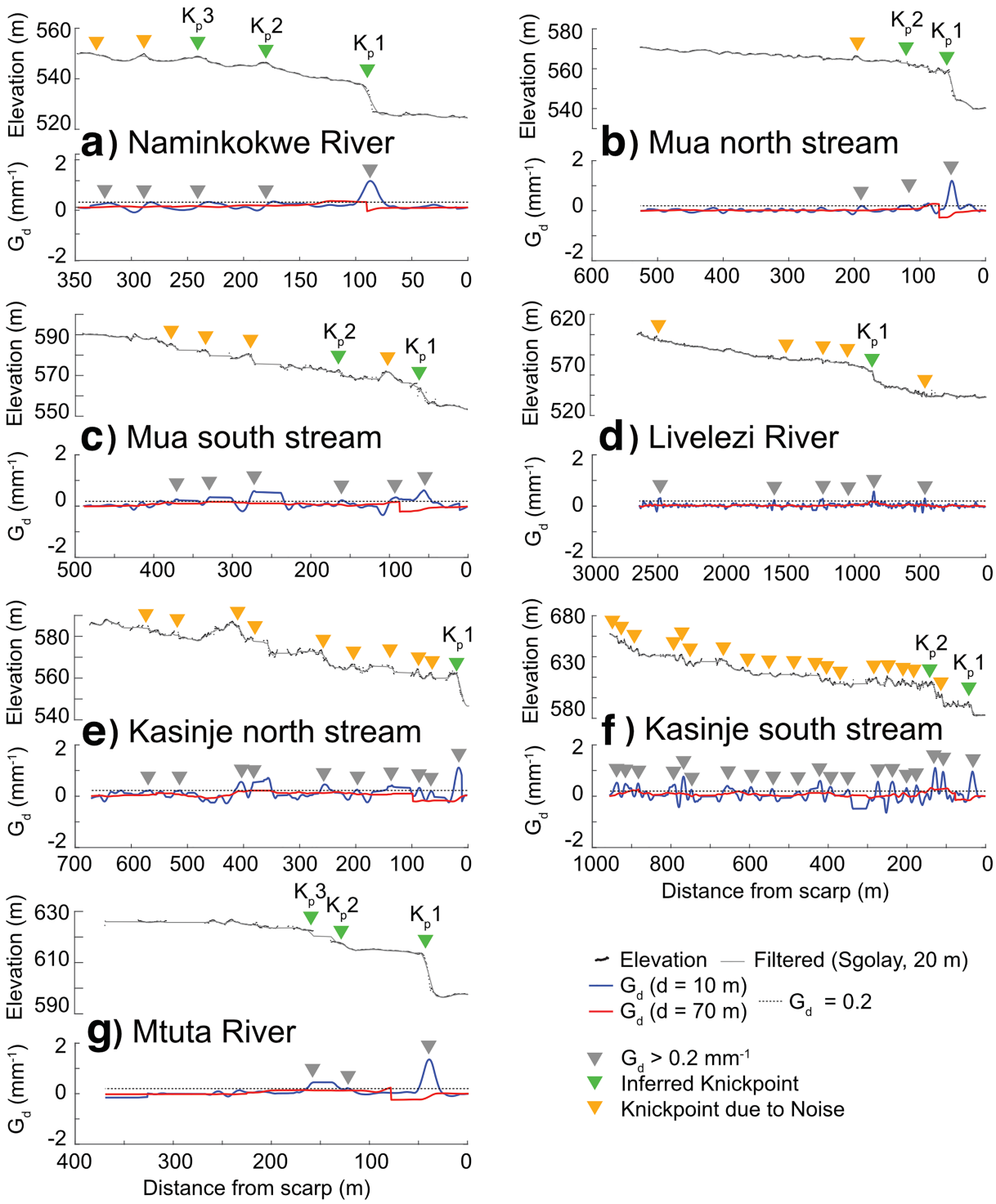

Figure 11. River and stream profiles for (a) Naminkokwe River, (b) Mua north stream, (c) Mua south stream, (d) Livelezi River, (e) Kasinje north stream, (f) Kasinje south stream, and (g) Mtuta River. Profile elevation (black circles) was filtered using the Savitzky-Golay digital filter and window size of 20 m. For the G_d plot, a d of 10 (blue) and 70 m (red) were used to identify knickpoints. The dotted black line indicates a G_d of 0.2. Knickpoints identified in the gradient G_d profile are shown as gray triangles. These were then quality checked and considered tectonic knickpoints (green triangles) or artifacts of noise (orange triangles). Knickpoints are numbered K_p1, K_p2, and so forth based on their distance from the scarp.

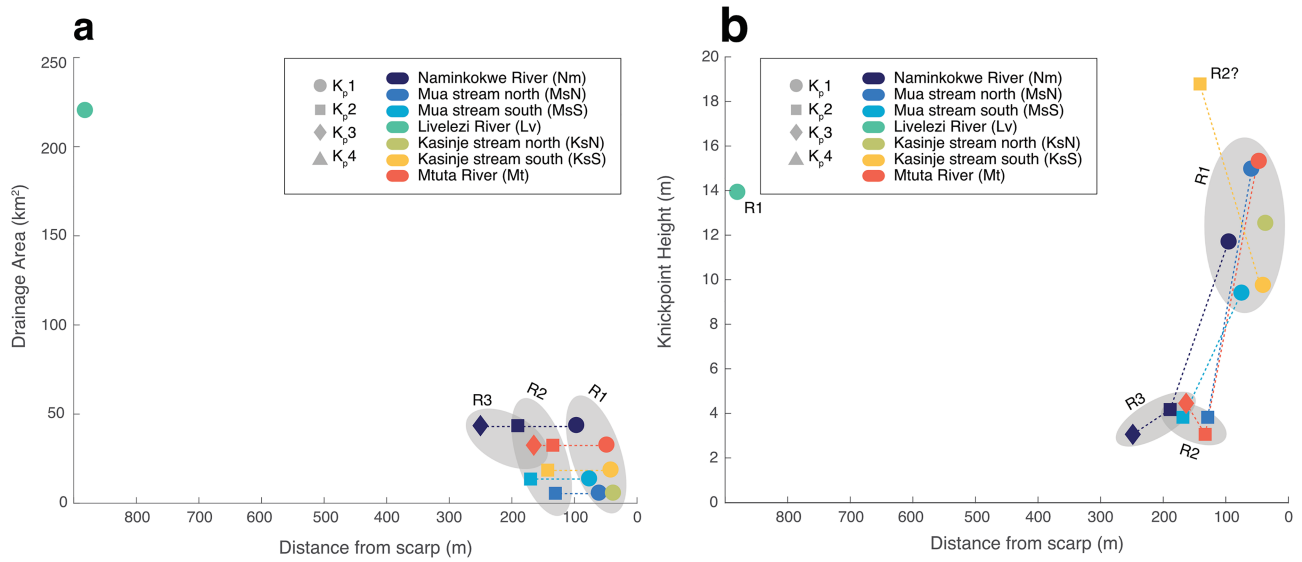

Figure 12. (a) Knickpoint distance from scarp versus drainage area. (b) Knickpoint distance from scarp versus scarp height.

6. Knickpoints

We calculate the gradient of each river profile using a rolling window of length d:

$$G_d = \frac{e_2 - e_1}{d}, \tag{3}$$

where e_1 and e_2 are elevations at $d/2$ either side of the measurement point, respectively. The value of G_d changes as a function of d in response to the local riverbed morphology (Wei et al., 2015). Here, we test a d of 10 and 70 m and find that the best value for our data is $d = 10$ m, but large knickpoints could still be identified using $d = 70$ m (Figure 10) . Attempts have been made to automate knickpoint identification using G_d (Hayakawa & Oguchi, 2006); however, choosing an appropriate threshold value to objectively define knickpoints is challenging for small drainage areas (Wei et al., 2015). Here, we choose $G_d > 0.2$ and manually analyze smaller peaks.

To identify which knickpoints are caused by faulting, we follow the criteria proposed by Wei et al. (2015): (1) Knickpoints are only considered if they are located upstream of the fault scarp (i.e., in the footwall); (2) we exclude candidates if the elevation fluctuates considerably on either side of the point; and (3) we use geological and topographical maps, to exclude points positioned at lithologic contacts, at the confluence of tributaries and/or bends in the river profile (Wohl, 1993). We note that regional geological maps may not account for local lithological variation, a possible source of error within the profiles. We number the knickpoints for each stream chronologically based on their distance from the scarp (i.e., K_p1, K_p2, … K_pn).

Each river or stream has at least one inferred knickpoint, K_p1 (Figure 11). The first knickpoint is well defined and is usually located within 100 m of the fault scarp. The larger distance of K_p1 on the Livelezi River (~900 m) may suggest that the retreat rate on the Livelezi is faster than the others, consistent with its larger discharge rate (assumed by its larger width) and drainage area (Berlin & Anderson, 2007; Bishop et al., 2005; Crosby & Whipple, 2006; Hayakawa & Oguchi, 2006; Seidl et al., 1994; e.g., Figure 12). The river with the second largest drainage area/discharge is the Naminkokwe River (Dawson & Kirkpatrick, 1968), whose K_p1 is setback the second furthest from the scarp (~95 m). A second knickpoint K_p2 was identified on five of the profiles (Naminkokwe and Mtuta rivers and both Mua streams and the northern Kasinje stream) but not on Livelezi River. Where identified, K_p2 is setback between 130 and 190 m from the scarp (Figure 10). A third knickpoint K_p3 was identified on both the Naminkokwe and Mtuta rivers and is setback 160 to 250 m from the scarp. The lack of additional knickpoints on the Livelezi River may be due to the larger catchment area and discharge rate causing knickpoints to migrate upstream at a faster rate, beyond the limits of our profile (Attal et al., 2011, 2008; Wallace, 1977; Whittaker et al., 2007a, 2007b, 2008).

To calculate the height of the knickpoints, we manually pick the top and bottom of the knickpoint, using the onset and end of the trough in the calculated profile gradient. We then fit a regression line through the upper

and lower surface and calculate the elevation difference between these regression lines at the center of the knickpoint. The location of the knickpoint is measured as the distance upstream from the scarp. The average height of K_p1 (green stars, Figure 8b) was 12 ±3 m on the Mua segment and 13 ± 3 m on the Kasinje segment. Additional knickpoints (K_p2 and K_p3) were typically lower, measuring around 5 m on average; however, K_p2 on the southern Kasinje stream measured 19 m in height, larger than the height of K_p1 measured along the stream (10 m).

The number of knickpoints corresponds well with number of subscarps identified on the scarp profiles and confirms that more than one rupture event has likely occurred on both the Mua and Kasinje segments of the Bilila-Mtakataka (Figure 8b). The clustering of K_p1 suggests they were formed by the same event: the last rupture event (R1). Similarly, we attribute the similar distances of K_p2 on all profiles (Figure 12) to be due to a concurrent or near concurrent, older rupture: the penultimate, observable surface rupturing event (R2). Along on the Naminkokwe and Mtuta rivers, which both have similar drainage areas (Figure 4), K_p3 are setback a similar distance. Furthermore, the knickpoint of the Mtuta River is situated a few kilometers south of where a third rupture event was found on Scarp Profile K12. Consequently, this third knickpoint may be representative of a potential third, older rupture (R3).

7. Discussion

7.1. Comparison Between Scarp and Knickpoint Analyses

Whereas previous analyses on the BMF have focused solely on the total scarp height (Hodge et al., 2019, 2018b), here using the high-resolution DEM created from Pleiades data, we were able to identify subscarps and estimate the incremental vertical surface displacements. While it is possible that multiple splays were active during a single event, the consistent pattern of vertical displacements along the length of the segments suggests these subscarps record separate earthquakes rather than local variations in geometry. The average scarp height of the most recent rupture event (R1) was ~12 m on both segments. The penultimate rupture event (R2) identified from the composite scarps and multiscarps had a similar scarp height (~11 m). The R1 and R2 scarp height profiles show variability along the segments, and there are significant gaps in where R2 was recorded due to noisy profiles. A third potential event recorded on K12 had a scarp height of 5 m, and it is likely that any evidence for older events will have been obscured by erosion. The total scarp heights broadly match previous results (Hodge et al., 2019, 2018b) and show that while there is an intense local variability in the scarp height along the BMF, the average total scarp height is over 20 m on both segments and is largest at the segment centers (Figure 8).

The height of individual knickpoints that have formed during consecutive ruptures may be a proxy for the vertical offset in each earthquake (Wei et al., 2015). We compare the cumulative knickpoint height measured from each river profile to the total scarp height measured from the closest scarp profile and find that the river profiles on average express 80% of the total scarp height. When comparing R1 knickpoint and scarp heights, the knickpoints record over 100% of the scarp height; as scarp height is locally variable, the closest scarp used here may not represent a larger scarp local to the knickpoint. The good correlation between knickpoint and scarp heights suggests that the well-defined first knickpoints (K1) are therefore likely true reflections of the latest vertical surface displacement from the most recent rupture on the two segments. The height of R2 from the river profiles is between 20% and 50% of the nearest R2 scarp height, when not including the abnormally large K2 height on the southern Kasinje stream. However, the nearest scarp profiles were all composite scarps, which may comprise additional ruptures that have been masked. When compared the R2 knickpoint height to the closest R2 scarp height from multiscarps, the knickpoints express between 55% and 80% of the vertical offset. The R3 knickpoint on the Mtuta River has a height that expresses 90% of the nearest R3 scarp height from a multiscarp.

The abnormally large knickpoint height of second knickpoint (~19 m) on the southern Kasinje stream, when compared to other K_p2 heights (<5 m), may be explained by a localized displacement high during an older event or the inability to distinguish multiple older ruptures. The nearest scarp profile was taken only a few hundred meters from the stream and shows evidence for an older rupture producing a ~16 m high scarp (Figure 8). Because these profiles are from the center of the Kasinje segment, this may imply that a larger displacement occurred here (conforming to a bell-shaped displacement profile); however, the large κt values from this region (Figure 9) may also suggest that older rupture markers may have been destroyed and that the scarp and knickpoint R2 may be formed from multiple, older events. In addition, the small discharge and catchment area for the southern Kasinje stream means that if a subsequent ruptures did occur here and

did so within a short enough period of time, a break in the longitudinal profile between knickpoints may not have developed.

7.2. Age Estimates

No historical rupture has been observed on the BMF, indicating that the most recent earthquake (R1) must have occurred over a hundred years ago (Hodge et al., 2015; Midzi et al., 1999). Our numerical model shows that even for regions with a small diffusion constant κ, a free face degrades and disappears within approximately a hundred years, consistent with our field and satellite observations. To remove individual event, markers on composite scarps required κt larger than 20 m^2, corresponding to a total time since formation of at least 2,000 to 4,000 years.

The estimated diffusion age of the Bilila-Mtakataka scarp is 48 ± 25 m^2, which corresponds to a total time since formation of 6.4 ± 4.0 Kyr, assuming a κ of 7.5 ± 2.5 m^2/Kyr. Assuming a constant κ for the entire scarp history may be invalid for regions where intense climatic variations occur over long time scales; however, drill cores from Lake Malawi suggest that the climatic conditions of Malawi have been relatively stable for the past 70,000 years Scholz et al. (2011). The range of estimates might therefore imply that sections of the Mua and Kasinje segments are several thousand years older than others and that the earlier earthquakes involved smaller segments rupturing independently. However, there was no correlation between diffusion age and scarp height (Figure 9c) nor is the distribution of knickpoints and scarp heights representative of multiple discontinuous ruptures. Instead, we suggest that the wide variation in diffusion age is related to local erosional processes (e.g., Kokkalas & Koukouvelas, 2005; i.e., variations in κ) including variations in properties of the fault damage zone associated with differences in the cross-cutting relationship between the scarp trend and the gneissic foliation (Hodge et al., 2018b).

The diffusion age for the Mua (52 ± 24 m^2) and Kasinje (42 ± 26 m^2) segments is the same within error, implying the scarps likely formed at similar points in time. Similarly, the consistent height of the R1 scarp implies that it formed in a single event across both segments. The fact that the R1 height does not decrease at the end of our study area suggests that it also propagated north onto the Mtakataka segment and south onto the Bilila segment. In contrast, the height of R2 scarp decreases at both the segment ends and the intersegment zone, suggesting separate ruptures of the Mua and Kasinje segments. Even ruptures ~20 km in length with 10 m of surface displacement would imply an unusually large slip-length ratio (5×10^{-4}) compared to global catalogs (Scholz, 2002). We therefore suggest that the R2 event ruptured both segments concurrent—or near concurrent—in time, as supported by the similar diffusion ages. The lack of a displacement low between the segments from R1, as seen in R2, may suggest the segments have become more mature in their structural linkage over recent earthquake cycles. Our findings suggest therefore that the BMF segments, over the last two earthquake cycles, have not ruptured individually. This finding profoundly influences the seismic hazard of the area, as it implies that the rupture length is not constrained by the structural segment lengths (Goda et al., 2018).

7.3. Magnitude Estimates

Using relationships between earthquake magnitude and the total average BMF scarp height (~14 m), previous studies had estimated that the scarp was formed by a M_W 7.9 to 8.4 event (Hodge et al., 2019; Jackson & Blenkinsop, 1997). However, in this study we have concluded that the BMF scarp actually formed through multiple ruptures. Assuming that the whole BMF scarp reflects two earthquakes (i.e., any older events no longer contribute significantly to the scarp height) and that there was no vertical erosion between these events, the average vertical displacement (i.e., throw) of each event is 7 ± 4 m. In using these surface measurements to estimate average coseismic displacement $\bar{D}_s$, we note that it has been practice to infer $\bar{D}_s$ both directly from throw (i.e., scarp height; DuRoss, 2008; Nicol et al., 2010; Schwartz & Coppersmith, 1984) or from projecting throw into the fault dip (Litchfield et al., 2018; Villamor & Berryman, 2001; Xu et al., 2018). We apply both approaches here, noting that for a reasonable fault dip ($60° \pm 5°$), our projected estimates of $\bar{D}_s$ are only slightly increased (8.1 ± 5.2 m).

Our new estimate of $\bar{D}_s$ results in a slip-length ratio α of $6.8 \pm 5.5 \times 10^{-5}$ for a complete BMF rupture (rupture length, 110 km), which is in accordance with global values (Scholz, 2002). However, we cannot exclude the possibility that the most recent BMF earthquake ruptured only the Kasinje and Mua segments, in which case $\bar{D}_s$ is 10 m, length ~ 40 km, and thus α is 2.5×10^{-4}. Applying the methodology of Jackson and Blenkinsop (1997) to calculate the magnitude of a complete BMF rupture, but with the revised value of $\bar{D}_s$, we calculate a range of magnitudes from M_W 7.7 to 8.3 (equation (1) and Table 1). Alternatively, we estimate the magnitude

Table 1
Earthquake Magnitude (Including Lower and Upper) Estimates Using L = 110 km (±2 km), $\bar{D}_s$ = 7 m (±4 m), G = 30 GPa (±5 GPa; Stein & Liu, 2009), and W = T^s/δ (Where Seismogenic Thickness T^s = 30 km ± 5 km; Jackson & Blenkinsop, 1993; and Dip δ = 60° ± 5°)

Eq No.	Description	Equation	Average M_W	M_W range
(1)	Normal fault slip[a]	$M_W = \frac{2}{3} \cdot \log(G\bar{D}_s LW) - 6.05$	8.0	7.7–8.3
(2)	All slip type[b]	$M_W = 6.93 + 0.82 \cdot \log(\bar{D}_s)$	7.6	7.3–7.9
(3)	Interplate dip-slip[c]	$M_W = 6.84 + 2.00 \cdot \log(\bar{D}_s)$	8.5	7.8–9.1
(4)	All slip type[d]	$M_W = 5.08 + 1.16 \cdot \log(L)$	7.5	7.4–7.5
(5)	Interplate dip-slip[d]	$M_W = 4.40 + 1.52 \cdot \log(L)$	7.5	7.5

[a]Jackson and Blenkinsop (1997). [b]Hanks and Kanamori (1979). [c]Wells and Coppersmith (1994). [d]Leonard (2010).

range for a complete BMF rupture of M_W 7.3 to 7.9 according to the $\bar{D}_s$ magnitude scaling law by Wells and Coppersmith (1994) (Table 1 and equation (2)) and M_W 7.8 to 9.1 according to the $\bar{D}_s$ magnitude scaling laws for interplate dip-slip faults of Leonard (2010) (Table 1 and equation (3)).

The Wells and Coppersmith (1994) magnitude estimates using $\bar{D}_s$ are therefore comparable to those estimated using their surface rupture length (L) scaling laws (Table 1 and equation (4)), which range between M_W 7.4 and 7.5 assuming a complete BMF rupture. However, the Leonard (2010) $\bar{D}_s$ magnitude scaling gives a larger M_W than the L magnitude scaling (M_W 7.5; Table 1 and equation (5)). This may be indicative of the fact that our estimates of α are either at the higher end of values proposed by Scholz (2002) or even greater; such high values of α have also been observed for other earthquakes, which like Malawi, are hosted in thick elastic crust (Rodgers & Little, 2006; Smekalin et al., 2010).

It is not possible to comment here further on which of the magnitude equations in Table 1 are most appropriate for the BMF, only to highlight the care that should be used when selecting earthquake scaling relationships (Stirling et al., 2013). Regardless, in either case, the estimated earthquake magnitude from a complete rupture of the BMF is slightly greater than the largest naturally recorded earthquake events on the EARS, the M_W 7.3 1910 Rukwa event (Ambraseys & Adams, 1991), the M_W 7.0 1990 Juba earthquake (Hartnady, 2002), and the M_W 7 2006 Machaze earthquake (Fenton & Bommer, 2006). Furthermore, the average M_W of 7.8 for a complete BMF rupture is slightly lower than previously estimated (Jackson & Blenkinsop, 1997) and is another example of where better constraining rupture slip has led to lower magnitude estimates (e.g., the 1739 Yinchuan earthquake, China; Middleton et al., 2016).

These calculations assume a characteristic earthquake model for the BMF, and while the geomorphological analysis in this study found no evidence for single segment ruptures along the Mua and Kasinje segments, multisegment ruptures may occur across both segments but not the entire fault. For example, the Citsulo segment may be a barrier to rupture propagation (Hodge et al., 2018b). Such ruptures would have a lower earthquake magnitude, due to the shorter rupture length, but also have a shorter recurrence interval. Complete and segmented ruptures along the BMF pose different seismic hazards for the region (Goda et al., 2018; Hodge et al., 2015). A detailed geomorphological analysis on the remaining BMF segments (Ngodzi, Mtakataka, Citsulo, and Bilila) is therefore required.

8. Conclusion

The ~110 km long BMF comprises a scarp whose average height (~14 m) exceeds that which would have formed from a single event, given global slip-length scaling laws (e.g., Scholz, 2002). Indeed, the two central structural segments—the Mua and Kasinje segments—have scarps more than 20 m high in places. Previous work has suggested that scarps of similar heights form through multiple ruptures on the same fault plane (a composite scarp) or unique near-surface fault planes (a multiscarp). Our numerical models of scarp diffusion show that multiscarps and composite scarps display differing morphological signatures.

By undertaking a geomorphological analysis of the fault scarps along the Mua and Kasinje segments, using a high-resolution DEM, we suggest there is evidence for at least two ruptures. A separate knickpoint analysis on three rivers and four streams that cross the fault scarp agree with these findings. By calculating the

individual vertical displacement of each rupture from the scarp and knickpoints, we estimate the average vertical surface displacement along the two segments to be ~10 m per rupture. Results from a scarp degradation model used to estimate diffusion age κt on each scarp profile, by finding a best fit to the current profile, imply that the most recent rupture was continuous across both structural segments and that the penultimate rupture was concurrent, or near-concurrent, in time across both segments. Extrapolating these findings for the entire BMF, we suggest that the surface slip per event is less than 10 m, as expected by global slip-length scaling laws, and that a complete rupture would equate to a M_W range of 7.5 to 8.1. This is likely smaller than previously suggested for the fault but greater than the largest earthquakes recorded along the entire EARS. We have demonstrated that high-resolution satellite topography can be used to identify surface ruptures from multiple earthquakes. This could be applied to other large, prehistoric normal fault scarps whose scarp height exceeds what would be anticipated by a single earthquake event (Scholz, 2002). Candidates for this include the Kanda fault, Lake Rukwa (Macheyeki et al., 2007; Vittori et al., 1997), the Nahef East fault, northern Israel (Mitchell et al., 2001), the Wasatch fault zone faults, Utah (DuRoss et al., 2015; Swan et al., 1980), and the Dixie Valley-Pleasant Valley faults (Zhang et al., 1991).

Acknowledgments
Michael Hodge is supported by the NERC GW4+ Doctoral Training Partnership (Grant Code NE/L002434/1) and Centre for Observation and Modelling of Earthquakes, Volcanoes and Tectonics (COMET). Juliet Biggs is supported by COMET and the NERC Large Grant Looking into Continents from Space (LiCS, NE/K010913/1). Juliet Biggs, Åke Fagereng, Luke Wedmore, and Jack Williams are supported by the EPSRC Global Challenges grant PREPARE (EP/P028233/1). Hassan Mdala acknowledges the Geological Survey Department, Malawi, for attaching him to the project. All authors acknowledge the Geological Survey Department, Malawi, for their assistance with fieldwork in Malawi. Pleiades data were obtained using a small grant from COMET and the point cloud data are available from opentopography.org: https://doi.org/10.5069/G92R3PSV (Mua section) and https://doi.org/10.5069/G96H4FJ1 (Kasinje section). We thank Dan Hobley and two anonymous reviewers for their helpful comments on drafts of this manuscript.

References

Ambraseys, N., & Adams, R. (1991). Reappraisal of major African earthquakes, south of 20°N, 1900–1930. *Natural Hazards*, *4*, 389–419. https://doi.org/10.1007/BF00126646

Anders, M. H., & Schlische, R. W. (1994). Overlapping faults, intrabasin highs, and the growth of normal faults. *The Journal of Geology*, *102*(2), 165–179. https://doi.org/10.1086/629661

Andrews, D. J., & Hanks, T. C. (1985). Scarp degraded by linear diffusion: Inverse solution for age. *Journal of Geophysical Research*, *90*(B12), 10,193–10,208.

Arrowsmith, J. R., Pollard, D. D., & Rhodes, D. D. (1996). Hillslope development in areas of active tectonics. *Journal of Geophysical Research*, *101*(B3), 6255–6275. https://doi.org/10.1029/95JB02583

Arrowsmith, J. R., Rhodes, D. D., & Pollard, D. D. (1998). Morphologic dating of scarps formed by repeated slip events along the San Andreas Fault, Carrizo Plain, California. *Journal of Geophysical Research*, *103*(B5), 10141–10160.

Attal, M., Cowie, P. A., Whittaker, A. C., Hobley, D., Tucker, G. E., & Roberts, G. P. (2011). Testing fluvial erosion models using the transient response of bedrock rivers to tectonic forcing in the Apennines, Italy. *Journal of Geophysical Research*, *116*, F02005. https://doi.org/10.1029/2010JF001875

Attal, M., Tucker, G. E., Whittaker, A. C., Cowie, P. A., & Roberts, G. P. (2008). Modelling fluvial incision and transient landscape evolution: Influence of dynamic channel adjustment. *Journal of Geophysical Research*, *113*, F03013. https://doi.org/10.1029/2007JF000893

Avouac, J.-p. (1993). Analysis of scarp profiles: Evaluation of errors in morphologic dating. *Journal of Geophysical Research*, *98*(B4), 6745–6754.

Avouac, J.-p., & Peltzer, G. (1993). Active tectonics in Southern Xinjiang, China: Analysis of terrace riser and normal fault scarp degradation along the Hotan-Qira Fault System. *Journal of Geophysical Research*, *98*(B12), 21,773–21,807.

Berlin, M. M., & Anderson, R. S. (2007). Modeling of knickpoint retreat on the Roan Plateau, western Colorado. *Journal of Geophysical Research*, *112*, F03S06. https://doi.org/10.1029/2006JF000553

Bishop, P., Hoey, T. B., Jansen, J. D., & Lexartza Artza, I. (2005). Knickpoint recession rate and catchment area: The case of uplifted rivers in Eastern Scotland. *Earth Surface Processes and Landforms*, *30*(6), 767–778. https://doi.org/10.1002/esp.1191

Bucknam, R. C., & Anderson, R. E. (1979). Estimation of fault-scarp ages from a scarp-height-slope-angle relationship. *Geology*, *7*, 11–14.

Burbank, D. W., & Anderson, R. S. (2011). *Tectonic geomorphology*. Blackwell Science.

Carretier, S., Ritz, J. F., Jackson, J., & Bayasgalan, A. (2002). Morphological dating of cumulative reverse fault scarps: Examples from the Gurvan Bogd fault system, Mongolia. *Geophysical Journal International*, *148*(2), 256–277. https://doi.org/10.1046/j.1365-246X.2002.01599.x

Castillo, M. (2017). Landscape evolution of the graben of Puerto Vallarta (west-central Mexico) using the analysis of landforms and stream long profiles. *Journal of South American Earth Sciences*, *73*, 10–21. https://doi.org/10.1016/j.jsames.2016.11.002

Cleveland, W. S. (1981). LOWESS: A program for smoothing scatterplots by robust locally weighted regression. *The American Statistician*, *35*(1), 54.

Commins, D., Gupta, S., & Cartwright, J. A. (2005). Deformed streams reveal growth and linkage of a normal fault array in the Canyonlands graben, Utah. *Geology*, *33*(8), 645–648. https://doi.org/10.1130/G21433.1

Cowie, P. A., Attal, M., Tucker, G. E., Whittaker, A. C., Naylor, M., Ganas, A., & Roberts, G. P. (2006). Investigating the surface process response to fault interaction and linkage using a numerical modelling approach. *Basin Research*, *18*(3), 231–266. https://doi.org/10.1111/j.1365-2117.2006.00298.x

Crone, A. J., & Haller, K. M. (1991). Segmentation and the coseismic behavior of Basin and Range normal faults: Examples from east-central Idaho and southwestern Montana, U.S.A. *Journal of Structural Geology*, *13*(2), 151–164. https://doi.org/10.1016/0191-8141(91)90063-O

Crosby, B. T., & Whipple, K. X. (2006). Knickpoint initiation and distribution within fluvial networks: 236 waterfalls in the Waipaoa River, North Island, New Zealand. *Geomorphology*, *82*(1-2), 16–38. https://doi.org/10.1016/j.geomorph.2005.08.023

Culling, W. E. H. (1963). Soil creep and the development of hillside slopes. *The Journal of Geology*, *71*(2), 127–161.

Dawson, A. L., & Kirkpatrick, I. K. (1968). *The geology of the Cape Maclear Peninsula and Lower Bwanje Valley* (Vol. 28). Malawi: Bulletin of the Geological Survey.

DuRoss, C. B. (2008). Holocene vertical displacement on the central segments of the Wasatch fault zone, Utah. *Bulletin of the Seismological Society of America*, *98*(6), 2918–2933. https://doi.org/10.1785/0120080119

DuRoss, C. B., Personius, S. F., Crone, A. J., Olig, S. S., Hylland, M. D., Lund, W. R., & Schwartz, D. P. (2015). Fault segmentation: New concepts from the Wasatch Fault Zone, Utah, USA. *Journal of Geophysical Research: Solid Earth*, *121*, 1131–1157. https://doi.org/10.1002/2015JB012419

Duffy, O. B., Brocklehurst, S. H., Gawthorpe, R. L., Leeder, M. R., & Finch, E. (2014). Controls on landscape and drainage evolution in regions of distributed normal faulting: Perachora Peninsula, Corinth Rift, Central Greece. *Basin Research*, *27*, 1–22. https://doi.org/10.1111/bre.12084

Dulanya, Z. (2017). A review of the geomorphotectonic evolution of the south Malawi rift. *Journal of African Earth Sciences*, *129*, 728–738.

Ebinger, C. (1989). Tectonic development of the western branch of the East African Rift System. *Geological Society of America Bulletin*, *101*, 885–903. https://doi.org/10.1130/0016-7606(1989)101h0885

Ebinger, C., Rosendahl, B., & Reynolds, D. (1987). Tectonic model of the Malawi rift, Africa. *Tectonophysics*, *141*, 215–235. http://www.sciencedirect.com/science/article/pii/0040195187901879

Elvidge, C. D., & Lyon, R. J. P (1985). Estimate of the vegetation contribution to the 1.65/2.22 m ratio in airborne thematic-mapper imagery of the Virginia Range, Nevada. *International Journal of Remote Sensing*, *6*, 75–88.

Ewiak, O., Victor, P., & Oncken, O. (2015). Investigating multiple fault rupture at the Salar del Carmen segment of the Atacama Fault System (northern Chile): Fault scarp morphology and knickpoint analysis. *Tectonics*, *34*, 187–212. https://doi.org/10.1002/2014TC003599

Fenton, C. H., & Bommer, J. J. (2006). The M_W7 Machaze, Mozambique, earthquake of 23 February 2006. *Seismological Research Letters*, *77*(4), 426–439.

Finlayson, D. P., Montgomery, D. R., & Hallet, B. (2002). Spatial coincidence of rapid inferred erosion with young metamorphic massifs in the Himalayas. *Geology*, *30*(3), 219–222. https://doi.org/10.1130/0091-7613(2002)030<0219:SCORIE>2.0.CO;2

Flannery, J., & Rosendahl, B. (1990). The seismic stratigraphy of Lake Malawi, Africa: Implications for interpreting geological processes in lacustrine rifts. *Journal of African Earth Sciences*, *10*(3), 519–548. http://www.sciencedirect.com/science/article/pii/089953629090104M

Fu, B., Ninomiya, Y., Lei, X., Toda, S., & Awata, Y. (2004). Mapping active fault associated with the 2003 Mw 6.6 Bam (SE Iran) earthquake with ASTER 3D images. *Remote Sensing of Environment*, *92*, 153–157. https://doi.org/10.1016/j.rse.2004.05.019

Ganas, A., Pavlides, S., & Karastathis, V. (2005). DEM-based morphometry of range-front escarpments in Attica, central Greece, and its relation to fault slip rates. *Geomorphology*, *65*, 301–319. https://doi.org/10.1016/j.geomorph.2004.09.006

Gasparini, N. M., Bras, R. L., & Whipple, K. X. (2006). Numerical modeling of non-steady river profile evolution using a sediment-flux-dependent incision model. *Geological Society of America Special Paper*, *398*(08), 127–141. https://doi.org/10.1130/2006.2398(08)

Giba, M., Walsh, J. J., & Nicol, A. (2012). Segmentation and growth of an obliquely reactivated normal fault. *Journal of Structural Geology*, *39*, 253–267. https://doi.org/10.1016/j.jsg.2012.01.004

Goda, K., Kloukinas, P., Risi, R., Hodge, M., Kafodya, I., Ngoma, I., et al. (2018). Scenario-based seismic risk assessment for Malawi using improved information on earthquake sources and local building characteristics. In *16th European Conference on Earthquake Engineering* (pp. 12). Greece: Springer Verlag.

Gomberg, J., Reasenberg, Pa, Bodin, P., & Harris, Ra (2001). Earthquake triggering by seismic waves following the Landers and Hector Mine earthquakes. *Nature*, *411*(6836), 462–466. https://doi.org/10.1038/35078053

Grigillo, D., Fras, M. K., & Petrovič, D. (2012). Automated building extraction from IKONOS images in suburban areas. *International Journal of Remote Sensing*, *33*(16), 5149–5170. https://doi.org/10.1080/01431161.2012.659356

Hanks, T. C., Bucknam, R. C., Lajoie, K. R., & Wallace, R. E. (1984). Modification of wave-cut and faulting-controlled landforms. *Journal of Geophysical Research*, *89*(10), 5771–5790. https://doi.org/10.1029/JB089iB07p05771

Hanks, T. C., & Kanamori, H. (1979). A moment magnitude scale. *Journal of Geophysical Research*, *84*(B5), 2348–2350.

Hartnady, C. (2002). Earthquake hazard in Africa: Perspectives on the Nubia-Somalia boundary: News and view. *South African journal of Science*, *98*, 425–428. http://reference.sabinet.co.za/sa_epublication_article/sajsci_v98_n9_10_a5

Hayakawa, Y. S., & Oguchi, T. (2006). DEM-based identification of fluvial knickzones and its application to Japanese mountain rivers. *Geomorphology*, *78*, 90–106.

Hayakawa, Y. S., & Oguchi, T. (2009). GIS analysis of fluvial knickzone distribution in Japanese mountain watersheds. *Geomorphology*, *111*, 27–37. https://doi.org/10.1016/j.geomorph.2007.11.016

He, Z., & Ma, B. (2015). Holocene paleoearthquakes of the Daqingshan fault detected from knickpoint identification and alluvial soil profile. *Journal of Asian Earth Sciences*, *98*, 261–271. https://doi.org/10.1016/j.jseaes.2014.11.025

Hodge, M., Biggs, J., Fagereng, Å., Elliott, A., Mdala, H., & Mphepo, F. (2019). A semi-automated algorithm to quantify scarp morphology (SPARTA): Application to normal faults in Southern Malawi. *Solid Earth*, *10*(1), 27–57.

Hodge, M., Biggs, J., Fagereng, A., & Mdala, H. (2018b). Controls on early-rift geometry: New perspectives from the Bilila-Mtakataka fault, Malawi. *Geophysical Research Letters*, *45*, 3896–3905. https://doi.org/10.1029/2018GL077343

Hodge, M., Biggs, J., Goda, K., & Aspinall, W. (2015). Assessing infrequent large earthquakes using geomorphology and geodesy: The Malawi Rift. *Natural Hazards*, *76*(3), 1781–1806. https://doi.org/10.1007/s11069-014-1572-y

Hodge, M., Fagereng, A., & Biggs, J. (2018a). The role of static stress changes during earthquakes in linking normal faults: Bend, growth, breached ramp or transform? *Journal of Geophysical Research: Solid Earth*, *123*, 797–814. https://doi.org/10.1002/2017JB014927

Holbrook, J., & Schumm, S. A. (1999). Geomorphic and sedimentary response of rivers to tectonic deformation: A brief review and critique of a tool for recognizing subtle epeirogenic deformation in modern and ancient settings. *Tectonophysics*, *305*(1-3), 287–306. https://doi.org/10.1016/S0040-1951(99)00011-6

Holland, W. N., & Pickup, G. (1976). Flume study of knickpoint development in stratified sediment. *Bulletin of the Geological Society of America*, *87*(1), 76–82. https://doi.org/10.1130/0016-7606(1976)87<76:FSOKDI>2.0.CO;2

Howard, A. D., & Kerby, G. (1983). Channel changes in badlands. *Geological Society of America Bulletin*, *94*(6), 739–752. https://doi.org/10.1130/0016-7606(1983)94<739:CCIB>2.0.CO;2

Jackson, J., & Blenkinsop, T. (1993). The Malawi earthquake of March 10, 1989: Deep faulting within the East Africa Rift System. *Tectonics*, *12*(5), 1131–1139.

Jackson, J., & Blenkinsop, T. (1997). The Bilila-Mtakataka fault in Malawi: An active, 100-km long, normal fault segment in thick seismogenic crust. *Tectonics*, *16*(1), 137–150.

Kokkalas, S., & Koukouvelas, I. K. (2005). Fault-scarp degradation modeling in central Greece: The Kaparelli and Eliki faults (Gulf of Corinth) as a case study. *Journal of Geodynamics*, *40*(2-3), 200–215. https://doi.org/10.1016/j.jog.2005.07.006

Kristensen, M. B., Childs, C. J., & Korstgard, J. A. (2008). The 3D geometry of small-scale relay zones between normal faults in soft sediments. *Journal of Structural Geology*, *30*(2), 257–272. https://doi.org/10.1016/j.jsg.2007.11.003

Laó-Dávila, D. A., Al-Salmi, H. S., Abdelsalam, M. G., & Atekwana, E. A. (2015). Hierarchical segmentation of the Malawi Rift: The influence of inherited lithospheric heterogeneity and kinematics in the evolution of continental rifts. *Tectonics*, *34*, 2399–2417. https://doi.org/10.1002/2015TC003953

Lee, J.-c., Chu, H.-t., Angelier, J., Chan, Y.-c., Hu, J.-c., Lu, C.-y., & Rau, R.-j. (2002). Geometry and structure of northern surface ruptures of the 1999 Mw 7.6 Chi-Chi Taiwan earthquake: Influence from inherited fold belt structures. *Journal of Structural Geology*, *24*, 173–192.

Leonard, M. (2010). Earthquake fault scaling: Self-consistent relating of rupture length, width, average displacement, and moment release. *Bulletin of the Seismological Society of America*, *100*(5A), 1971–1988. https://doi.org/10.1785/0120090189

Leopold, L. B., & Maddock, T. (1953). *The hydraulic geometry of stream channels and some physiographic implications*, vol. 252. Washington: US Government Printing Office.

Lin, A., Sano, M., Wang, M., Yan, B., Bian, D., Fueta, R., & Hosoya, T. (2017). Paleoseismic study of the Kamishiro Fault on the northern segment of the Itoigawa–Shizuoka Tectonic Line, Japan. *Journal of Seismology*, *21*(4), 683–703. https://doi.org/10.1007/s10950-016-9629-x

Litchfield, N. J., Campbell, J. K., & Nicol, A. (2003). Recognition of active reverse faults and folds in North Canterbury, New Zealand, using structural mapping and geomorphic analysis. *New Zealand Journal of Geology and Geophysics*, *46*(4), 563–579.

Litchfield, N. J., Villamor, P., van Dissen, R. J., Nicol, A., Barnes, P. M., Barrell, D. J. A., et al. (2018). Surface rupture of multiple crustal faults in the 2016 Mw7.8 Kaikōura, New Zealand, earthquake. *Bulletin of the Seismological Society of America*, *108*(3B), 1496–1520. https://doi.org/10.1785/0120170300

Macheyeki, AS, Delvaux, D., Kervyn, F., Petermans, T., & Verbeeck, K. (2007). Occurrence of large earthquakes along the major Kanda fault system (Tanganyika-Rukwa rift, SW highlands of Tanzania). *Geophysical Research Abstracts*, *9*, 9–10.

Mackenzie, D., & Elliott, A. (2017). Untangling tectonic slip from the potentially misleading effects of landform geometry. *Geosphere*, *13*(4), 1310–1328. https://doi.org/10.1130/GES01386.1

Manighetti, I., Campillo, M., Sammis, C., Mai, P. M., & King, G. (2005). Evidence for self-similar, triangular slip distributions on earthquakes: Implications for earthquake and fault mechanics. *Journal of Geophysical Research*, *110*, B05302. https://doi.org/10.1029/2004JB003174

Manighetti, I., King, G. C. P., & Gaudemer, Y. (2001). Slip accumulation and lateral propagation of active normal faults in Afar. *Journal of Geophysical Research*, *106*(B7), 13,667–13,696.

Mayer, L. (1982). Quantitative tectonic geomorphology with applications to neotectonics of Northwestern Arizona (PhD Thesis). http://hdl.handle.net/10150/187532

McCalpin, J. P. (2009). *Paleoseismology* (Vol. 95). Dordrecht: Academic press.

Michetti, M., & Brunamonte, F. (1996). Trench investigations of the 1915 Fucino earthquake fault scarps (Abruzzo, central Italy): Geological evidence of large historical events. *Journal of Geophysical Research*, *101*, 5921–5936.

Middleton, T. A., Walker, R. T., Parsons, B., Lei, Q., Zhou, Y., & Ren, Z. (2016). A major, intraplate, normal-faulting earthquake: The 1739 Yinchuan event in northern China. *Journal of Geophysical Research: Solid Earth*, *121*, 293–320. https://doi.org/10.1002/2015JB012355

Midzi, V., Hlatywago, D. J., Chapola, L. S., Kebede, F., Atakan, K., Lombe, D. K., et al. (1999). Seismic hazard assessment in Eastern and Southern Africa. *Annali Di Geofisica*, *42*(6), 1067–1083.

Mitchell, S. G., Matmon, A., Bierman, R., Enzel, Y., Caffee, M., & Rizzo, D. (2001). Displacement history of a limestone normal fault scarp, northern Israel, from cosmogenic ^{36}Cl. *Journal of Geophysical Research*, *106*, 4247–4264.

Montgomery, D. R., & Brandon, M. T. (2002). Topographic controls on erosion rates in tectonically active mountain ranges. *Earth and Planetary Science Letters*, *201*(3-4), 481–489. https://doi.org/10.1016/S0012-821X(02)00725-2

Morewood, N. C., & Roberts, G. P. (2001). Comparison of surface slip and focal mechanism slip data along normal faults: An example from the eastern Gulf of Corinth, Greece. *Journal of Structural Geology*, *23*, 473–487. https://doi.org/10.1016/S0191-8141(00)00126-7

Mueller, K. J., & Rockwell, T. K. (1995). Late Quaternary activity of the Laguna Salada fault in northern Baja California, Mexico. *Geological Society of America Bulletin*, *107*(1), 8–18. https://doi.org/10.1130/0016-7606(1995)107<0008:LQAOTL>2.3.CO;2

Nash, D. B. (1980). Morphologic dating of degraded normal fault scarps. *The Journal of Geology*, *88*(3), 353–360.

Nash, D. B. (1984). Morphologic dating of fluvial terrace scarps and fault scarps near West Yellowstone, Montana. *Geological Society of America Bulletin*, *95*(12), 1413–1424. https://doi.org/10.1130/0016-7606(1984)95<1413:MDOFTS>2.0.CO;2

Nicol, A., Walsh, J., Villamor, P., Seebeck, H., & Berryman, K. (2010). Normal fault interactions, paleoearthquakes and growth in an active rift. *Journal of Structural Geology*, *32*(8), 1101–1113. https://doi.org/10.1016/j.jsg.2010.06.018

Niviére, B., & Marquis, G. (2000). Evolution of terrace risers along the upper Rhine graben inferred from morphologic dating methods: Evidence of climatic and tectonic forcing. *Geophysical Journal International*, *141*(3), 577–594. https://doi.org/10.1046/j.1365-246X.2000.00123.x

Ouchi, S. (1985). Response of alluvial rivers to slow active tectonic movement. *Geological Society of America Bulletin*, *96*, 504–515. https://doi.org/10.1130/0016-7606(1985)96<504:ROARTS>2.0.CO;2

Palyvos, N., Pantosti, D., De Martini, P. M., Lemeille, F., Sorel, D., & Pavlopoulos, K. (2005). The Aigion-Neos Erineos coastal normal fault system (western Corinth Gulf Rift, Greece): Geomorphological signature, recent earthquake history, and evolution. *Journal of Geophysical Research*, *110*, B09302. https://doi.org/10.1029/2004JB003165

Perrin, C., Manighetti, I., Ampuero, Jean-paul, Cappa, F., & Gaudemer, Y. (2016a). Location of largest earthquake slip and fast rupture controlled by along-strike change in fault structural maturity due to fault growth. *Journal of Geophysical Research: Solid Earth*, *121*, 3666–3685. https://doi.org/10.1002/2015JB012671

Perrin, C., Manighetti, I., & Gaudemer, Y. (2016b). Off-fault tip splay networks: A genetic and generic property of faults indicative of their long-term propagation. *Comptes Rendus Geoscience*, *348*, 52–60.

Peters, G., & van Balen, R. T. (2007). Tectonic geomorphology of the northern Upper Rhine Graben, Germany. *Global and Planetary Change*, *58*, 310–334. https://doi.org/10.1016/j.gloplacha.2006.11.041

Philippon, M., Willingshofer, E., Sokoutis, D., Corti, G., Sani, F., Bonini, M., et al. (2015). Slip re-orientation in oblique rifts. *Geology*, *43*(2), 1–4. https://doi.org/10.1130/G36208.1

Rawat, J. S., & Joshi, R. C. (2012). Remote-sensing and GIS-based landslide-susceptibility zonation using the landslide index method in Igo River Basin, Eastern Himalaya, India. *International Journal of Remote Sensing*, *33*(12), 3751–3767. https://doi.org/10.1080/01431161.2011.633121

Rodgers, D. W., & Little, T. A. (2006). World's largest coseismic strike-slip offset: The 1855 rupture of the Wairarapa Fault, New Zealand, and implications for displacement/length scaling of continental earthquakes. *Journal of Geophysical Research*, *111*, B12408. https://doi.org/10.1029/2005JB004065

Rosenbloom, N. A., & Anderson, R. S. (1994). Hillslope and channel evolution in a marine terraced landscape, Santa Cruz, California. *Journal of Geophysical Research*, *99*(94), 13–14. https://doi.org/10.1029/94JB00048

Saria, E., Calais, E., Stamps, DS, Delvaux, D., & Hartnady, CJH (2014). Present-day kinematics of the East African Rift. *Journal of Geophysical Research: Solid Earth*, *119*, 3584–3600. https://doi.org/10.1002/2013JB010901

Savitzky, A., & Golay, M. J. E. (1964). Smoothing and differentiation of data by simplified least squares procedures. *Analytical Chemistry*, *36*(8), 1627–1639. https://doi.org/10.1021/ac60214a047

Scholz, C. (2002). *The mechanics of earthquakes and faulting*. Cambridge: Cambridge university press.

Scholz, C., Cohen, A. S., Johnson, T. C., King, J., Talbot, M. R., & Brown, E. T. (2011). Scientific drilling in the Great Rift Valley: The 2005 Lake Malawi Scientific Drilling Project—An overview of the past 145,000 years of climate variability in Southern Hemisphere East Africa. *Palaeogeography, Palaeoclimatology, Palaeoecology*, *303*, 3–19. https://doi.org/10.1016/j.palaeo.2010.10.030

Schwartz, D. P., & Coppersmith, K. J. (1984). Fault behavior and characteristic earthquakes: Examples from the Wasatch and San Andreas Fault Zones. *Journal of Geophysical Research*, *89*, 5681–5698. https://doi.org/10.1029/JB089iB07p05681

Segall, P., & Pollard, D. D. (1983). Nucleation and growth of strike slip faults in granite. *Journal of Geophysical Research*, *88*, 555–568.

Seidl, M. A., Dietrich, W. E., & Kirchner, J. W. (1994). Longitudinal profile development into bedrock: An analysis of Hawaiian channels. *The Journal of Geology*, *102*(4), 457–474. https://doi.org/10.1086/629686

Slemmons, D. B. (1957). Geological effects of the Dixie Valley-Fairview Peak Nevada, Earthquakes of December 16, 1954. *Bulletin of the Seismological Society of America*, *47*(1934), 353–357.

Smekalin, O., Chipizubov, A., & Imaev, V. (2010). Paleoearthquakes in the Baikal region: Methods and results of timing. *Geotectonics*, *44*(2), 158–175. https://doi.org/10.1134/S0016852110020056

Smith, T. R., & Bretherton, F. P. (1972). Stability and the conservation of mass in drainage basin evolution. *Water Resources Research*, *8*(6), 1506–1529.

Stamps, D., Saria, E., & Kreemer, C. (2018). A geodetic strain rate model for the East African Rift System. *Scientific Reports*, *8*(1), 732.

Stein, S., & Liu, M. (2009). Long aftershock sequences within continents and implications for earthquake hazard assessment. *Nature*, *462*(7269), 87–89.

Stirling, M., Goded, T., Berryman, K., & Litchfield, N. (2013). Selection of earthquake scaling relationships for seismic-hazard analysis. *Bulletin of the Seismological Society of America*, *103*(6), 2993–3011. https://doi.org/10.1785/0120130052

Sun, C., Wan, T., Xie, X., Shen, X., & Liang, K. (2016). Knickpoint series of gullies along the Luoyunshan Piedmont and its relation with fault activity since late Pleistocene. *Geomorphology*, *268*, 266–274. https://doi.org/10.1016/j.geomorph.2016.06.026

Swan, F. H., Schwartz, D. P., & Cluff, L. S. (1980). Recurrence of moderate to large magnitude earthquakes produced by surface faulting on the Wasatch Fault Zone, Utah. *Bulletin of the Seismological Society of America*, *70*(5), 1431–1462.

Villamor, P., & Berryman, K. (2001). A late Quaternary extension rate in the Taupo Volcanic Zone, New Zealand, derived from fault slip data. *New Zealand Journal of Geology and Geophysics*, *44*(2), 243–269. https://doi.org/10.1080/00288306.2001.9514937

Vittori, E., Delvaux, D., & Kervyn, F. (1997). Kanda fault: A major seismogenic element west of the Rukwa Rift (Tanzania, East Africa). *Journal of Geodynamics*, *24*, 139–153. https://doi.org/10.1016/S0264-3707(96)00038-5

Walker, R. T., Wegmann, K. W., Bayasgalan, A., Carson, R. J., Elliott, J., Fox, M., et al. (2015). The Egiin Davaa prehistoric rupture, central Mongolia: A large magnitude normal faulting earthquake on a reactivated fault with little cumulative slip located in a slowly deforming intraplate setting. *Seismicity, Fault Rupture and Earthquake Hazards in Slowly Deforming Regions*, *432*, 187–212. https://doi.org/10.1144/SP432.4

Wallace, R. E. (1977). Profiles and ages of young fault scarps, north-central Nevada. *Geological Society of America Bulletin*, *88*, 1267–1281.

Wallace, R. E. (1980). Degradation of the Hebgen Lake fault scarps of 1959. *Geology*, *8*(5), 225–229. https://doi.org/10.1130/0091-7613(1980)8<225:DOTHLF>2.0.CO

Wallace, R. E. (1984). *Fault scarps formed during the earthquakes of October 2, 1915, in Pleasant Valley, Nevada, and some tectonic implications*, U.S. Geological Survey Professional Paper 1274-A. Washington, DC: US Government Printing Office.

Walshaw, R. D. (1965). The geology of the Ncheu-Balaka area. *Bulletin of the Geological Survey, Malawi*, *19*, 96.

Wei, Z., Bi, L., Xu, Y., & He, H. (2015). Evaluating knickpoint recession along an active fault for paleoseismological analysis: The Huoshan Piedmont, Eastern China. *Geomorphology*, *235*, 63–76. https://doi.org/10.1016/j.geomorph.2015.01.013

Wells, D., & Coppersmith, K. (1994). New empirical relationships among magnitude, rupture length, rupture width, rupture area, and surface displacement. *Bulletin of the Seismological Society of America*, *84*(4), 974–1002. http://bssa.geoscienceworld.org/content/84/4/974.short

Whipple, K. X., & Tucker, G. E. (1999). Dynamics of the stream-power river incision model: Implications for height limits of mountain ranges, landscape response timescales, and research needs. *Journal of Geophysical Research*, *104*(B8), 17,661–17,674.

Whittaker, A. C., Attal, M., Cowie, P. A., Tucker, G. E., & Roberts, G. (2008). Decoding temporal and spatial patterns of fault uplift using transient river long profiles. *Geomorphology*, *100*(3-4), 506–526. https://doi.org/10.1016/j.geomorph.2008.01.018

Whittaker, A. C., Cowie, P. A., Attal, M., Tucker, G. E., & Roberts, G. P. (2007a). Contrasting transient and steady-state rivers crossing active normal faults: New field observations from the Central Apennines, Italy. *Basin Research*, *19*(4), 529–556. https://doi.org/10.1111/j.1365-2117.2007.00337.x

Whittaker, A. C., Cowie, P. A., Attal, M., Tucker, G. E., & Roberts, G. P. (2007b). Bedrock channel adjustment to tectonic forcing: Implications for predicting river incision rates. *Geology*, *35*(2), 103–106. https://doi.org/10.1130/G23106A.1

Willemse, E. J. M., & Pollard, D. D. (1998). On the orientation and patterns of wing cracks and solution surfaces at the tips of a sliding flaw or fault. *Journal of Geophysical Research: Solid Earth*, *103*, 2427–2438. https://doi.org/10.1029/97JB01587

Williams, J. N., Fagereng, Å., Wedmore, L. N. J., Biggs, J., Mphepo, F., Dulanya, Z., et al. (2019). How do variably striking faults reactivate during rifting? Insights from southern Malawi. *Geochemistry, Geophysics, Geosystems*, *20*, 3588–3607. https://doi.org/10.1029/2019GC008219

Wohl, E. E. (1993). Bedrock channel incision along Piccaninny Creek, Australia. *The Journal of Geology*, *101*(6), 749–761.

Wu, D., & Bruhn, R. L. (1994). Geometry and kinematics of active normal faults, South Oquirrh Mountains, Utah: Implication for fault growth. *Journal of Structural Geology*, *16*(8), 1061–1075. https://doi.org/10.1016/0191-8141(94)90052-3

Xu, Y., He, H., Deng, Q., Allen, M. B., Sun, H., & Bi, L. (2018). The CE 1303 Hongdong earthquake and the Huoshan Piedmont Fault, Shanxi Graben: Implications for magnitude limits of normal fault earthquakes. *Journal of Geophysical Research: Solid Earth*, *123*, 3098–3121. https://doi.org/10.1002/2017JB014928

Yang, J., Guo, Z., & Cao, J. (1985). Investigation on the Holocene activities of the Helan mountain piedmont fault by use of geomorphological method. *Seismology and Geology (in Chinese with English abstract)*, *7*(4), 23–31.

Yu, L., Porwal, A., Holden, E.-J., & Dentith, M. C. (2011). Suppression of vegetation in multispectral remote sensing images. *International Journal of Remote Sensing*, *32*(22), 7343–7357. https://doi.org/10.1080/01431161.2010.523726

Zhang, P., Slemmons, D. B., & Mao, F. (1991). Geometric pattern, rupture termination and fault segmentation of the Dixie Valley-Pleasant Valley active normal fault system, Nevada, U.S.A. *Journal of Structural Geology*, *13*(2), 165–176. http://www.sciencedirect.com/science/article/pii/019181419190064P

Zielke, O., Klinger, Y., & Arrowsmith, J. R. (2015). Fault slip and earthquake recurrence along strike-slip faults—Contributions of high-resolution geomorphic data. *Tectonophysics*, *638*(1), 43–62. https://doi.org/10.1016/j.tecto.2014.11.004

Zielke, O., & Strecker, M. R. (2009). Recurrence of large earthquakes in magmatic continental rifts: Insights from a paleoseismic study along the Laikipia-Marmanet fault, Subukia Valley, Kenya rift. *Bulletin of the Seismological Society of America*, *99*(1), 61–70. https://doi.org/10.1785/0120080015